

Models of binary neutron star remnants with tabulated equations of state

Panagiotis Iosif¹★ and Nikolaos Stergioulas¹

¹*Department of Physics, Aristotle University of Thessaloniki, Thessaloniki 54124, Greece*

Accepted XXX. Received YYY; in original form ZZZ

ABSTRACT

The emergence of novel differential rotation laws that can reproduce the rotational profile of binary neutron star merger remnants has opened the way for the construction of equilibrium models with properties that resemble those of remnants in numerical simulations. We construct models of merger remnants, using a recently introduced 4-parameter differential rotation law and three tabulated, zero-temperature equations of state. The models have angular momenta that are determined by empirical relations, constructed through numerical simulations. After a systematic exploration of the parameter space of merger remnant equilibrium sequences, which includes the determination of turning points along constant angular momentum sequences, we find that a particular rotation law can reproduce the threshold mass to prompt collapse to a black hole with a relative difference of only $\sim 1\%$ with respect to numerical simulations, in all cases considered. Furthermore, our results indicate a possible correlation between the compactness of equilibrium models of remnants at the threshold mass and the compactness of maximum-mass nonrotating models. Another key prediction of binary neutron star merger simulations is a relatively slowly rotating inner region, where the angular velocity Ω (as measured by an observer at infinity) is mostly due to the frame dragging angular velocity ω . In our investigation of the parameter space of the adopted differential rotation law, we naturally find quasi-spherical (Type A) remnant models with this property. Our investigation clarifies the impact of the differential rotation law and of the equation of state on key properties of binary neutron star remnants and lays the groundwork for including thermal effects in future studies.

Key words: stars: neutron – stars: rotation – methods: numerical – relativistic processes – stars: kinematics and dynamics – equation of state

1 INTRODUCTION

The detection of gravitational waves (GW) from the inspiral phase of the GW170817 binary neutron star (BNS) merger event (Abbott et al. 2017a; Abbott et al. 2017b) combined with complementary information from its electromagnetic counterpart (Abbott et al. 2017b,c; Goldstein et al. 2017) have produced new constraints on the equation of state (EOS), see Bauswein et al. (2017); Abbott et al. (2018); De et al. (2018); Fattoyev et al. (2018); Most et al. (2018); Abbott et al. (2019); Montaña et al. (2019); Capano et al. (2020); Landry et al. (2020); Dietrich et al. (2020); Breschi et al. (2021) and references therein, as well as Chatziioannou (2020); Dietrich et al. (2021) for recent reviews. A second likely BNS merger event, GW190425, was reported in Abbott et al. (2020b) and more are expected in the next years (Abbott et al. 2020a). Although the sensitivity of the LIGO and Virgo GW detectors was not sufficient to detect the post-merger phase in GW170817 (Abbott et al. 2017a,d), such a detection is likely to be achieved in the future, either with upgraded or next-generation detectors, see e.g. Clark et al. (2014, 2016); Chatziioannou et al. (2017); Bose et al. (2018); Yang et al. (2018); Torres-Rivas et al. (2019); Martynov et al. (2019); Oliver et al. (2019); Easter et al. (2019); Tsang et al. (2019); Breschi et al. (2019); Hall & Evans (2019); Easter et al. (2020); Ackley et al. (2020); Haster et al. (2020); Aggarwal et al. (2021); Ganapathy et al. (2021); Page et al. (2021).

The outcome of a BNS merger is closely tied to the EOS and the total mass $M = m_1 + m_2$ of the system, where m_1 and m_2 are the binary’s components masses, see Shibata & Hotokezaka (2019); Bernuzzi (2020); Radice et al. (2020); Friedman & Stergioulas (2020) for recent reviews. If $M < M_{\text{thres}}$ (the threshold mass for prompt black hole formation), the merger results in a hot, massive and differentially rotating, compact object with a substantial material disk around it. If, at the same time, $M > M_{\text{max,rot}}$ (the maximum mass of a cold, uniformly rotating neutron star), the remnant will initially survive several tens of milliseconds (ms) due to the support of differential rotation and thermal pressure. However, the loss of angular momentum, due to GW emission, as well as dissipative effects (e.g. shear viscosity, magnetic breaking and effective viscosity due to the development of the magneto-rotational instability, see Shibata & Hotokezaka (2019); Cioffi (2020); Sarin & Lasky (2021); Ruiz et al. (2021) for recent reviews and also Radice 2020) will ultimately lead to a delayed collapse to a black hole. A remnant with mass $M_{\text{max,rot}} > M > M_{\text{max}}$, where M_{max} is the maximum mass of a nonrotating star, will be long-lived, spinning down on the timescale of electromagnetic emission, before reaching the axisymmetric instability limit. Only if $M < M_{\text{max}}$, can a stable remnant form.

During the first few milliseconds after its formation, the remnant is still highly non-axisymmetric, featuring also strong nonlinear oscillations and deformations away from equilibrium. Characteristic nonlinear features are combination tones and spiral deformations (Stergioulas et al. 2011; Bauswein & Stergioulas 2015; Bauswein et al. 2016; Bauswein & Stergioulas 2019). On a somewhat longer

★ E-mail: piosif@auth.gr

timescale, one can regard the remnant as a quasi-stationary, slowly drifting equilibrium state with the addition of linear oscillations. If one neglects some aspects of the state of the remnant (non-axisymmetric deformations, oscillations, time-dependence and thermal structure), one can construct simplified, stationary axisymmetric models of its structure.

Merger remnants that survive for more than a few milliseconds before collapsing to black holes have been studied through numerical simulations (Hotokezaka et al. 2011; Sekiguchi et al. 2011; Bauswein & Janka 2012; Bauswein et al. 2012; Hotokezaka et al. 2013; Bernuzzi et al. 2014; Dietrich et al. 2015; De Pietri et al. 2016; Radice et al. 2018). The remnant’s structure, including its rotation profile was studied extensively in Kastaun & Galeazzi (2015); Paschalidis et al. (2015); Bauswein & Stergioulas (2015); Kastaun et al. (2016); East et al. (2016); Endrizzi et al. (2016); Kastaun et al. (2017); Ciolfi et al. (2017); Hanauske et al. (2017); Endrizzi et al. (2018); Kiuchi et al. (2018); Ciolfi et al. (2019); East et al. (2019); De Pietri et al. (2020); Kastaun & Ohme (2021). A common finding is that the remnant’s rotation profile exhibits a maximum away from the center, which is in sharp disagreement with the differential rotation law by Komatsu et al. (1989), hereafter KEH, which was widely used in the context of differentially rotating neutron stars (see Ansorg et al. 2009; Espino & Paschalidis 2019; Espino et al. 2019 for different types of equilibrium models that can be constructed with the KEH rotation law).

A 3-parameter piecewise extension of the KEH rotation law was used in Bauswein & Stergioulas (2017); Bozzola et al. (2018), in order to allow the outer regions to rotate more slowly than the core, reaching high masses (typical of remnants) without encountering mass-shedding (see also Galeazzi et al. (2012); Uryū et al. (2016) for other rotation laws). Two different 3-parameter and 4-parameter rotation laws were proposed by Uryū et al. (2017), who presented selected example equilibrium models.

Zhou et al. (2019) constructed differentially rotating strange star models, using the 4-parameter rotation law of Uryū et al., whereas Passamonti & Andersson (2020) and Xie et al. (2020) studied the onset of the low $T/|W|$ instability (Watts et al. 2005) in models constructed with the 3-parameter rotation law of Uryū et al. In Camelió et al. (2021) models of stationary remnants of a BNS merger at $\sim 10 - 50$ ms after merger were presented, which were differentially rotating, hot, and baroclinic, using their own, 5-parameter rotation law. The models were constructed with the assumption of spatial conformal flatness (IWM-CFC approximation).

An important aspect of modeling post-merger remnants is to separate the effects of i) the differential rotation law, ii) the cold part of the EOS, and iii) thermal effects on the structure of the remnant and on its dynamical properties (stability to axisymmetric collapse and oscillations). To do so, we embarked on a systematic study of each of these three effects in separation from the other two. Our first step was to present equilibrium sequences of rotating relativistic stars, constructed with the 4-parameter rotation law of Uryū et al., adopting a cold, relativistic $N = 1$ polytropic EOS and choosing rotational parameters motivated by simulations of binary neutron star merger remnants (Iosif & Stergioulas 2021). A distinctive feature of the Uryū et al. law is that it allows for the angular velocity to attain a maximum value Ω_{\max} away from center (as seen in simulations), which was not possible with the KEH law. We compared the sequences of equilibrium models to published sequences that used the KEH rotation law, revealing only a small influence of the choice of rotation law on the mass of the equilibrium models and a somewhat larger influence on their radius. Both Type A and Type C solutions (in correspondence to the classification of KEH-type models by Ansorg et al. 2009) were

found. While our models were highly accurate solutions of the fully general relativistic structure equations, we also demonstrated that for models relevant to merger remnants the IWM-CFC approximation still maintains an acceptable accuracy.

Here, we take a second step in this program and construct sequences of models of post-merger remnants, using the 4-parameter rotation law of Uryū et al. and different tabulated EOS. In Bauswein & Stergioulas (2017) the threshold mass to black hole collapse, as determined in simulations, was reproduced in a semi-analytic way, using equilibrium models obeying a piecewise extension of the KEH rotation law. Following the analysis detailed in that work, our sequences are constructed using an empirical relation between angular momentum at merger and the radius and compactness of the progenitor stars (assuming equal masses). Again, we find both Type A and Type C sequences. For a particular combination of rotation-law parameters, we find that the sequence of merger remnants terminates very near the threshold mass to collapse (as obtained by numerical simulations) for all three representative EOS that we used in this study. For somewhat different combinations of rotation-law parameters, we find sequences of merger remnants with realistic rotation profiles, for which the angular velocity in the core is close to the angular velocity of frame dragging, reproducing a characteristic feature seen in binary neutron star merger simulations. The next step in this program will be the inclusion of thermal effects, which we are planning to present in the future.

The structure of the paper is as follows: in Section 2 we discuss the theoretical framework and numerical methods. In Section 3 we present the main results. In Section 4 we discuss our findings.

Throughout the text we set $c = G = 1$ in equations (except for equations where units are explicitly included) and choose appropriate physical units to report numerical results. We also denote with R_X the radius of nonrotating neutron stars with gravitational mass $X M_\odot$. E.g. $R_{1.4}$ stands for the radius of a $1.4 M_\odot$ star.

2 THEORETICAL FRAMEWORK AND METHODS

2.1 Spacetime metric and matter description

Our solutions are fully general relativistic, axisymmetric, and asymptotically flat and we adopt the following form of the line element, in quasi-isotropic coordinates:

$$ds^2 = -e^{\gamma+\rho} dt^2 + e^{\gamma-\rho} r^2 \sin^2 \theta (d\phi - \omega dt)^2 + e^{2\mu} (dr^2 + r^2 d\theta^2), \quad (1)$$

where γ , ρ , ω and μ are metric functions that depend only on the coordinates r and θ . The metric function ω is the angular velocity of a zero-angular-momentum-observer (ZAMO) and describes the relativistic dragging of inertial frames due to rotation.

The matter is described as a perfect fluid with a stress-energy tensor of the form

$$T^{\alpha\beta} = (\epsilon + P)u^\alpha u^\beta + P g^{\alpha\beta}, \quad (2)$$

where ϵ is the energy density, P is the pressure, u^α is the four-velocity of the fluid and $g_{\alpha\beta}$ is the metric tensor. Further details on the basic equations and concepts can be found in Friedman & Stergioulas (2013); Paschalidis & Stergioulas (2017).

2.2 Rotation law

The 1-parameter rotation law of Komatsu et al. (1989) (suitable for rotating proto-neutron stars formed after core-collapse) is

$$F(\Omega) = A^2(\Omega_c - \Omega), \quad (3)$$

where $F \equiv u^t u_\phi$ is the gravitationally redshifted angular momentum per unit rest mass and enthalpy and Ω_c is the angular velocity at the center of the star. In (3) the parameter A determines the length scale over which the angular velocity Ω changes.

In contrast, the 4-parameter rotation law of Uryū et al. (2017) reads

$$\Omega = \Omega_c \frac{1 + \left(\frac{F}{B^2 \Omega_c}\right)^p}{1 + \left(\frac{F}{A^2 \Omega_c}\right)^{q+p}}, \quad (4)$$

(hereafter Uryū+ law). As in Iosif & Stergioulas (2021), here we also fix two of the four parameters to the specific values $p = 1$ and $q = 3$. On one hand, setting integer values for p and q allows us to obtain an algebraic expression for the first integral of the hydrostationary equilibrium equation. On the other hand, fixing two of the four parameters allows us to investigate in detail a more manageable two-parameter space. The choice of $q = 3$ is motivated by the fact that for this value the rotation law tends to the Keplerian law at a large distance from the center, in the Newtonian limit.

As in Uryū et al. (2017) and Zhou et al. (2019), instead of investigating different values for the parameters A and B , we choose to work with the parameters

$$\lambda_1 \equiv \frac{\Omega_{\max}}{\Omega_c}, \quad (5)$$

$$\lambda_2 \equiv \frac{\Omega_e}{\Omega_c}, \quad (6)$$

where Ω_e is the angular velocity at the equator. This has the advantage of choosing parameter values that can be directly set by inspecting the ratios of Ω_{\max} and Ω_e with respect to Ω_c , as obtained in numerical simulations of BNS remnants. Note that all angular velocities are defined with respect to an observer at infinity.

2.3 Numerical scheme

In order to build our equilibrium configurations we use an extended version of the RNS code (Stergioulas & Friedman 1995), which implements the iterative Komatsu et al. (1989) scheme with improvements by Cook et al. (1992). The initial RNS code was updated to tackle differential rotation in Stergioulas et al. (2004) and further extended for the 3-parameter, piecewise KEH law in Bauswein & Stergioulas (2017). In Iosif & Stergioulas (2021), we extended RNS with the implementation of the 4-parameter Uryū+ rotation law of Eq. (4). This allowed for the construction of models with realistic rotation profiles for BNS merger remnants that have off-center maxima in the angular velocity profile. The solutions were shown to be highly accurate and converging at second order with an increasing number of grid points. A standard resolution was chosen that yields solutions with 3-dimensional virial theorem index (GRV3) of order 10^{-5} . In the present study, we employ a grid size of SDIV \times MDIV = 401 \times 201 (compactified radial times angular) for all models. We refer to Iosif & Stergioulas (2021) for further details on the numerical scheme.

2.4 Equations of state

Considerable uncertainty still exists in the determination of the EOS of dense nuclear matter. Figure 1 shows the gravitational mass M vs. the circumferential radius R for nonrotating models constructed with several different hadronic EOS that cover the large uncertainty

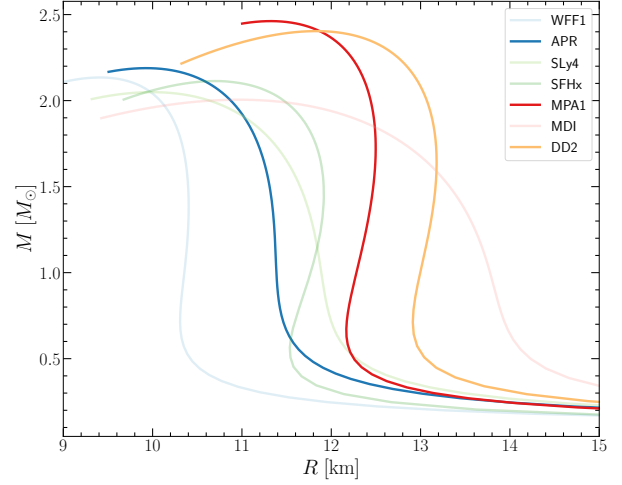


Figure 1. Gravitational mass M vs. circumferential radius R of nonrotating models for different EOS.

range that existed before the historic detection of gravitational waves from the source GW170817. The initial analysis of GW170817 resulted in a constraint on neutron star radii $R = 11.9^{+1.4}_{-1.4}$ km (Abbott et al. 2018) for both stars involved in the merger, at the 90% credible level. In the meantime, a large number of studies presented multi-messenger constraints on the neutron star radius, taking into account observations in the electromagnetic spectrum as well as nuclear-theory computations using chiral effective field theory. Recent studies provide predictions for the radius of a $1.4M_\odot$ neutron star with an uncertainty range of $R_{1.4} = 12.32^{+1.09}_{-1.47}$ km (90% credible level) (Landry et al. 2020), $R_{1.4} = 11.0^{+0.9}_{-0.6}$ km (90% credible level) (Capano et al. 2020), $R_{1.4} = 11.75^{+0.86}_{-0.81}$ km (90% credible level) (Dietrich et al. 2020), $R_{1.4} = 12.2^{+0.5}_{-0.5}$ km (1σ level) (Breschi et al. 2021) and $R_{1.4} = 11.94^{+0.76}_{-0.87}$ km (90% credible level) (Pang et al. 2021). Furthermore, the Neutron Star Interior Composition Explorer (NICER, Gendreau et al. 2016) measurements of PSR J0740+6620 have yielded radius estimates of $R_{1.4} = 12.45^{+0.65}_{-0.65}$ km (1σ level) (Miller et al. 2021), $R_{1.4} = 12.33^{+0.76}_{-0.81}$ km (95% credible level) and $R_{1.4} = 12.18^{+0.56}_{-0.79}$ km (95% credible level) for different high-density EOS parameterizations (Riley et al. 2021; Raaijmakers et al. 2021).

Taking into account the above range of radii uncertainties, we selected three tabulated, zero-temperature, hadronic EOS that correspond to typical neutron star radii between 11 and 13 km. These are APR (Akmal et al. 1998; Baym et al. 1971; Douchin & Haensel 2001), DD2 (Hempel & Schaffner-Bielich 2010; Typel et al. 2010; Möller et al. 1997) and MPA1 (Müther et al. 1987), shown with darker colors in Figure 1. All three EOS satisfy the current constraints for the maximum neutron star mass (Demorest et al. 2010; Antoniadis et al. 2013; Cromartie et al. 2020) as well as the minimum radius constraint, when combining causality and GW170817, of $R_{1.6} \geq 10.68$ km (Bauswein et al. 2017). EOS with strong phase transitions are not included in the present study.

2.5 Construction of merger remnant sequences

Our aim is to construct sequences of equilibrium models that mimic characteristic properties of post-merger remnants and reach the threshold mass to prompt collapse.

In Bauswein & Stergioulas (2017) an empirical, EOS-insensitive relation that connects the angular momentum at merger J_{merger} to the

total mass of a binary neutron star system M_{tot} was constructed:

$$\frac{cJ_{\text{merger}}}{GM_{\odot}^2} \simeq a \frac{M_{\text{tot}}}{M_{\odot}} - \left(b + \frac{R_{1.5} - R_{1.5}^{\text{DD2}}}{10 \text{ km}} \right), \quad (7)$$

where $a = 4.041$ and $b = 4.658$. An alternative relation was constructed by [Lucca et al. \(2021\)](#), who expressed J_{merger} as a function of the radius R_{NS} and compactness $C_{\text{NS}} = GM_{\text{NS}}/c^2 R_{\text{NS}}$ of a non-rotating neutron star with mass $M_{\text{NS}} = M_{\text{tot}}/2$

$$\frac{GJ_{\text{merger}}}{c^3 R_{\text{NS}}^2} = a_1 C_{\text{NS}} + a_2, \quad (8)$$

where $a_1 = 0.8765 \pm 0.0051$ and $a_2 = -(5.209 \pm 0.077) \times 10^{-2}$ (1σ credible level). We find that the two empirical relations are in good agreement with each other (see Appendix A for a comparison of the two relations' predictions). Note that both (7) and (8) have been derived by analyzing different sets of numerical simulations assuming equal mass binaries.

We construct sequences of models of merger remnants with different combinations of $\{\lambda_1, \lambda_2\}$ and with remnant masses of $M_{\text{tot}} = \{2.2, 2.3, 2.4, 2.5, \dots\} M_{\odot}$. We continue to larger values with a step of $0.1 M_{\odot}$ up to the maximum possible M_{tot} for which we can construct an equilibrium sequence for the particular rotation law and EOS. For each value of M_{tot} , we compute the corresponding R_{NS} and M_{NS} of a nonrotating star. From (8) we compute the corresponding angular momentum of the remnant. The detailed properties of the equilibrium models of merger remnant sequences are reported in Tables 5, 6 and 7 and they are discussed in detail in Section 3.

2.6 Constant angular momentum sequences and turning points

For each merger remnant model, we also construct the corresponding sequence of equilibrium models with the same rotation law and fixed J_{merger} . In the case of uniform rotation, the line connecting the turning points of each constant angular momentum sequence, i.e. the points where

$$\left. \frac{dM}{d\epsilon_{\text{max}}} \right|_{J=\text{const.}} = 0, \quad (9)$$

(where ϵ_{max} is the maximum value of the energy density in the star) defines the secular instability limit to axisymmetric perturbations ([Friedman et al. 1988](#)). Note that the turning point criterion is only a sufficient condition for secular instability of uniformly rotating stars.

The dynamical instability to prompt collapse to a black hole is detected through numerical simulations or by finding the models for which the frequency of the fundamental quasi-radial mode vanishes. For uniform rotation, the dynamical instability limit for prompt collapse is very close to the secular instability limit and it occurs slightly earlier (see [Friedman & Stergioulas \(2013\)](#) for a detailed discussion). In the case of differential rotation, [Weih et al. \(2018\)](#) demonstrated (through numerical simulations) that for particular choices of the KEH law the dynamical instability also sets in very close to the secular instability limit (the central density of dynamically unstable models was at most several percent smaller than the central density at the turning points).

Given the above findings for uniformly rotating as well as differentially rotating models with the KEH law and since we don't yet have dynamical or perturbative calculations for models constructed with the Uryu+ law, we adopt the line connecting the turning points of constant angular momentum sequences as a reasonably *approximate* indicator of dynamical instability.

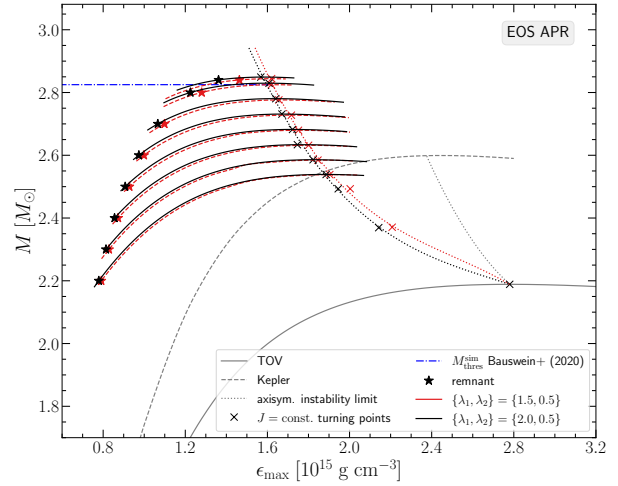


Figure 2. Gravitational mass M vs. maximum energy density ϵ_{max} for the APR EOS. Two choices of rotation law parameters yielding Type C solutions are shown. The nonrotating (TOV) sequence (grey solid line), the mass-shedding (Kepler) limit for uniform rotation (grey dashed line) and the axisymmetric instability limit for uniform rotation (grey dotted line) are shown as reference.

3 MAIN RESULTS

3.1 Sequences of Type C models and threshold mass to prompt collapse

Initially, we focus on two combinations of $\{\lambda_1, \lambda_2\}$ that were shown ([Iosif & Stergioulas 2021](#)) to yield Type C solutions according to the classification of [Ansorg et al. \(2009\)](#). These are sequences along which the models transition continuously from quasi-spherical to quasi-toroidal configurations, as the polar to equatorial axis ratio r_p/r_e is decreased. We find that setting parameters $\{\lambda_1, \lambda_2\}$ equal to the pairs of values $\{2.0, 0.5\}$ and $\{1.5, 0.5\}$, continues to result in Type C solutions for the tabulated EOS we examined, as was the case for the $N = 1$ polytropes in [Iosif & Stergioulas \(2021\)](#).

As can be seen in Figure 2 for the APR EOS, the J -constant curves for both of these rotation laws are overlapping and the turning points we locate are quite close as well. This is to be expected, as these two particular rotation laws correspond to similar $\Omega(r)$ rotational profiles ([Iosif & Stergioulas 2021](#), Figure 8). Asterisks in black and red denote the remnant models found for the respective J_{merger} values predicted by the empirical relation (8). The gravitational masses of these configurations for the APR EOS start at $2.2 M_{\odot}$ for the least massive model and end at $2.84 M_{\odot}$ for the most massive model (Table 5). The picture is similar for the other two EOS we consider, DD2 (see Figure 3 and Table 6) and MPA1 (see Figure 4 and Table 7). The only difference is that higher masses (as well as higher angular momentum values) are reached for the most massive remnant models at $3.28 M_{\odot}$ for DD2 and at $3.2 M_{\odot}$ for MPA1.

Qualitatively, the remnant sequence rises to larger masses at an almost constant (steep) slope that after a point abruptly diminishes, allowing the remnant sequence to intersect with the turning point line. As in [Bauswein & Stergioulas \(2017\)](#), we find that this intersection is related to the threshold mass for prompt collapse, $M_{\text{thres}}^{\text{sim}}$ (as determined by numerical simulations in [Bauswein et al. 2020](#)). This mass is indicated by a blue horizontal dash-dotted line in Figures 2, 3, 4, 8, 9 and 10. The intersection can also be determined in Figures 5, 6 and 7, which show the angular momentum J as a function of the gravitational mass M of the remnant sequence (blue line)

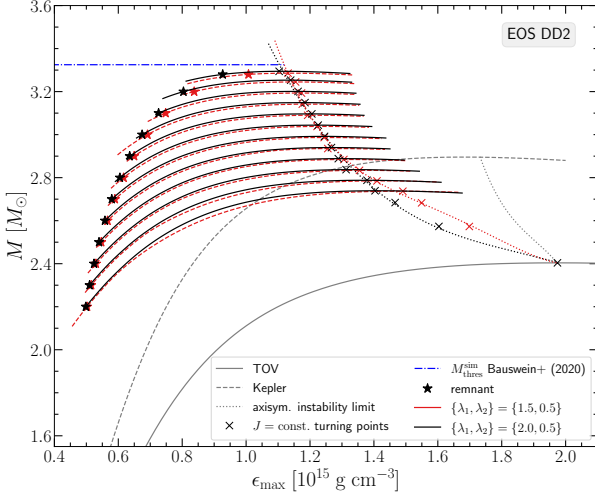


Figure 3. Same as Figure 2 for the DD2 EOS.

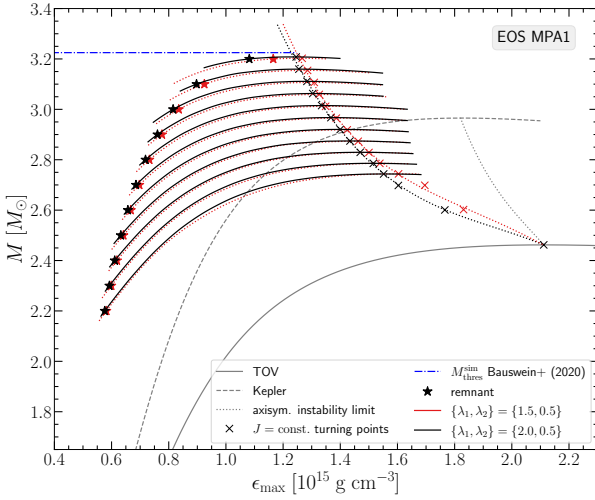


Figure 4. Same as Figure 2 for the MPA1 EOS.

and the line connecting the turning points of J -constant sequences for $\{\lambda_1, \lambda_2\} = \{2.0, 0.5\}$ (black line) and $\{\lambda_1, \lambda_2\} = \{1.5, 0.5\}$ (red line), for the three EOS. Note that the data for the remnant sequences in Figures 5, 6 and 7, as obtained from the empirical relation (8), form a straight line, in agreement with the form of the original empirical relation (7).

To locate the intersection point of the remnant sequence with the turning points line, we calculate linear fits for the remnant models and the turning points. These linear relations have the form

$$J = aM - b. \quad (10)$$

For the remnant sequences, this also facilitates a direct comparison between the J_{merger} empirical relations (7) and (8). In essence, (10) casts (8) in the form of (7). The coefficients a and b of these linear fits are reported in Table 1, together with their respective errors δa and δb .

The values of $M_{\text{thres}}^{\text{eq}}$ determined from the intersections of the linear fits for the remnant sequence and each turning point sequence in Figure 5, 6 and 7 are in excellent agreement with published values for the respective quantity $M_{\text{thres}}^{\text{sim}}$ from numerical simula-

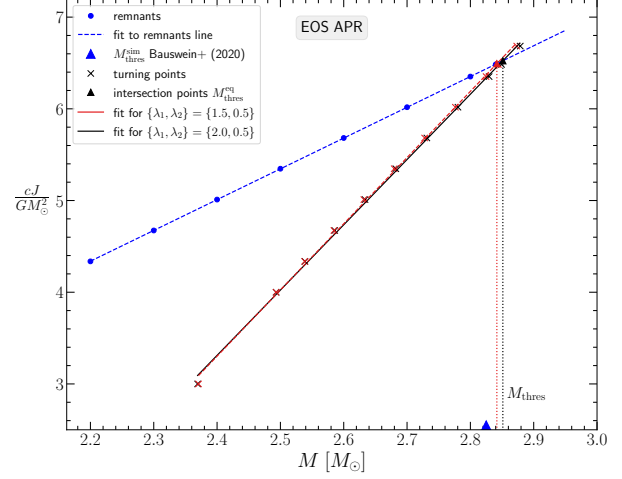


Figure 5. Angular momentum J vs. gravitational mass M for the APR EOS. The intersection of the remnants' and the turning points' fitted lines determines the threshold mass to collapse calculated from our equilibrium models, $M_{\text{thres}}^{\text{eq}}$.

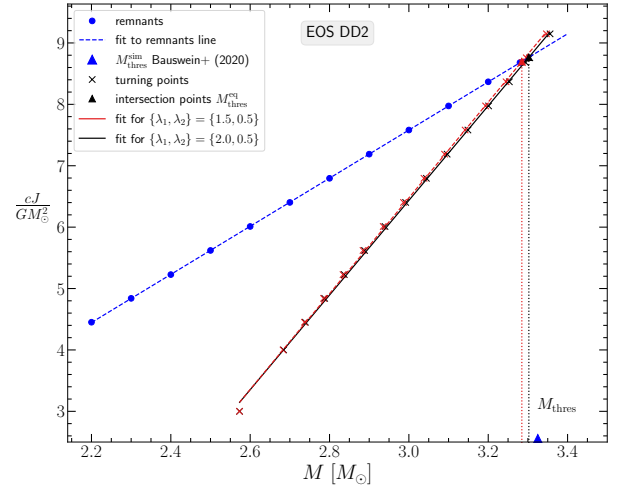


Figure 6. Same as Figure 5 for the DD2 EOS.

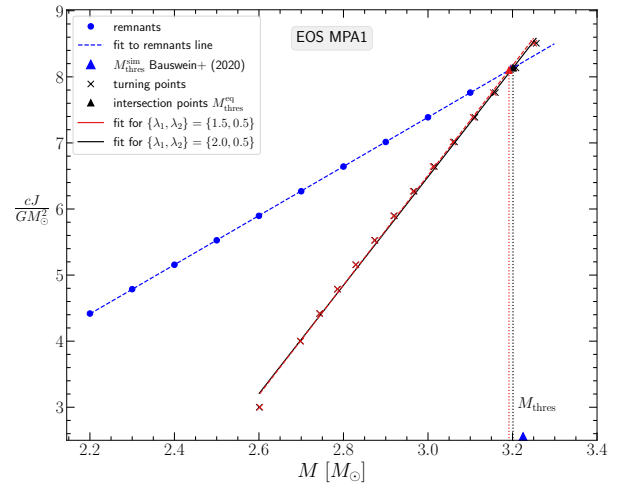


Figure 7. Same as Figure 5 for the MPA1 EOS.

Table 1. Coefficients of the linear fits $J = aM - b$ and their respective errors, that determine the intersection of the remnants sequence and the turning points line for each EOS (Figures 5, 6 and 7). The abbreviations RL, TP20 and TP15 stand for "remnant line" and "turning point line" with $\{\lambda_1, \lambda_2\} = \{2.0, 0.5\}$ and $\{\lambda_1, \lambda_2\} = \{1.5, 0.5\}$ respectively. The errors in the coefficients of the linear fits, δa and δb , are calculated with the standard formulas of simple linear regression and correspond to uncertainties at the 1σ level.

EOS	line	a	b	δa	δb
APR	RL	3.3562	3.0453	0.0027	0.0069
	TP20	7.1189	13.7739	0.0823	0.2220
	TP15	7.2199	14.0254	0.0827	0.2209
DD2	RL	3.9190	4.1758	0.0022	0.0062
	TP20	7.7087	16.6908	0.0523	0.1580
	TP15	7.8003	16.9247	0.0530	0.1597
MPA1	RL	3.7183	3.7673	0.0029	0.0079
	TP20	8.2014	18.1185	0.1116	0.3294
	TP15	8.3019	18.3962	0.1103	0.3253

tions (Bauswein et al. 2020, Supplementary Material)¹. For the case $\{\lambda_1, \lambda_2\} = \{2.0, 0.5\}$ we find $M_{\text{thres}}^{\text{eq}} = \{2.851, 3.302, 3.201\}$, which is to be compared to $M_{\text{thres}}^{\text{sim}} = \{2.825, 3.325, 3.225\}$, for the EOS APR, DD2 and MPA1 correspondingly (see Table 2). We also report the relative difference between $M_{\text{thres}}^{\text{eq}}$ and $M_{\text{thres}}^{\text{sim}}$ for each EOS and rotation law as

$$\delta M_{\text{thres}} = \left| \frac{M_{\text{thres}}^{\text{sim}} - M_{\text{thres}}^{\text{eq}}}{M_{\text{thres}}^{\text{sim}}} \right|. \quad (11)$$

The agreement with the threshold mass values from numerical simulations is at the 1% level, which is quite remarkable, considering that we only use *zero-temperature* EOS in constructing our models. A possible explanation is that in the case of prompt collapse, the kinetic energy of the collision does not have enough time to be transformed into thermal energy, through shock heating. Therefore, it would be the cold part of the EOS that mainly determines the properties of prompt collapse. We elaborate more on this topic on Section 4.

Also, the agreement at the level of 1% between our current models and numerical simulations is a significant improvement with respect to the agreement at the level of 3% - 7% in Bauswein & Stergioulas (2017), where a particular 3-parameter piecewise KEH-type rotation law was used. This is achieved without a direct reconstruction of particular merger remnants (i.e. without trying to match all properties of a remnant, as extracted from a numerical simulation), but using equilibrium models for particular $\{\lambda_1, \lambda_2\}$ values, in conjunction with the empirical relation for the angular momentum at merger.

The above findings indicate that the Uryu+ law is not simply qualitatively appropriate for merger remnants, in the sense that it allows for the maximum angular velocity to appear off-center, but it can also yield precise numerical results, at least for certain properties of the remnants.

3.2 Domain of Type A solutions

Merger remnants that do not collapse promptly, can evolve towards nearly axisymmetric, quasi-stationary configurations (at least before a possible delayed collapse sets in) that can be approximated with

Table 2. Comparison of the threshold mass deduced from equilibrium models $M_{\text{thres}}^{\text{eq}}$ with the respective quantity $M_{\text{thres}}^{\text{sim}}$ from the numerical simulations of Bauswein et al. (2020). The angular momentum value we find at the intersection point, $J_{\text{thres}}^{\text{eq}}$, is also reported. The last column lists the absolute value of the relative difference δM_{thres} calculated via (11).

EOS	$M_{\text{thres}}^{\text{eq}}$	$J_{\text{thres}}^{\text{eq}}$	$M_{\text{thres}}^{\text{sim}}$	δM_{thres}
$\{\lambda_1, \lambda_2\}$	$[M_{\odot}]$	$[\frac{GM_{\odot}^2}{c}]$	$[M_{\odot}]$	[%]
APR			2.825	
$\{2.0, 0.5\}$	2.851	6.524		0.92
$\{1.5, 0.5\}$	2.842	6.492		0.60
DD2			3.325	
$\{2.0, 0.5\}$	3.302	8.766		0.69
$\{1.5, 0.5\}$	3.285	8.697		1.20
MPA1			3.225	
$\{2.0, 0.5\}$	3.201	8.136		0.74
$\{1.5, 0.5\}$	3.192	8.100		1.02

suitable equilibrium models. This involves Type A solutions², i.e. sequences of models that remain quasi-spherical (the maximum density is always at the center) as the axis ratio r_p/r_e is decreased (i.e. the rotation rate increases) until the mass-shedding limit is reached.

In our recent work Iosif & Stergioulas (2021), we found that the Uryu+ rotation law with $\{\lambda_1, \lambda_2\} = \{2.0, 1.0\}$ and with $\{\lambda_1, \lambda_2\} = \{1.5, 1.0\}$ yields Type A solutions for the $N = 1$ polytropic EOS. In addition, we highlighted the fact that according to recent numerical simulations (Hanauske et al. 2017; De Pietri et al. 2020), a value of $\lambda_2 = 1$ seems to be favoured over $\lambda_2 = 0.5$, for the case of compact remnants from BNS mergers, while λ_1 ranges between 1.7-1.9 for realistic EOS. We therefore probe in more detail models with this range of parameters. To that end, we set the value of λ_2 to 1.0 and explore the range $\lambda_1 \in [1.5, 2.0]$ with a step of 0.1.

A vertical "scan" of the mass vs. ϵ_{max} parameter space for specific Type A $\{\lambda_1, \lambda_2\}$ pairs (fixing the value of the maximum energy density and gradually decreasing the axis ratio r_p/r_e), revealed that these sequences reached a point, after which it was not possible to further construct equilibrium solutions as the maximum density was increased. This behavior is much more stark for the case of $\{\lambda_1, \lambda_2\} = \{2.0, 1.0\}$ than for $\{\lambda_1, \lambda_2\} = \{1.5, 1.0\}$. We note that the terminal models encountered for each choice of $\{\lambda_1, \lambda_2\}$ pairs are not close to mass-shedding. For the highest $\{\lambda_1, \lambda_2\} = \{2.0, 1.0\}$, the Ω_e/Ω_K ratio of the terminal models ranges between 0.6-0.7 as the angular momentum increases, whereas for $\{\lambda_1, \lambda_2\} = \{1.5, 1.0\}$ it ranges between 0.6-0.8. However, the maximum density remained at the center of the configuration even at the highest rotation rates that were achieved and we classify these models as Type A.

Figure 8 displays the six Type A remnant sequences corresponding to the six $\{\lambda_1, \lambda_2\}$ pairs that we investigated³ for the APR EOS. Remnant models are shown as asterisks (different colors correspond to different $\{\lambda_1, \lambda_2\}$ values). The terminal models along each J -constant sequence for each $\{\lambda_1, \lambda_2\}$ pair are shown as dots of matching color. We find that the choice of $\lambda_1 = 1.6$ allows for the most massive Type A remnant model for this EOS, with a gravitational mass of $M_{\text{tot}} = 2.7M_{\odot}$.

For the $\{\lambda_1, \lambda_2\} = \{1.5, 1.0\}$ and $\{\lambda_1, \lambda_2\} = \{1.6, 1.0\}$ cases

¹ We note that in the simulations of Bauswein et al. (2020) the EOS table used for DD2 provided temperature dependence, whereas the APR and MPA1 were used in a hybrid form (zero-temperature EOS supplemented by an approximate thermal part).

² We use the same nomenclature as the classification of Ansong et al. (2009) for models constructed with the KEH rotation law.

³ As a related remark, see also Tsokaros et al. (2020, Figure 1) for the behavior of the turning points for different parameter choices with the KEH rotation law.

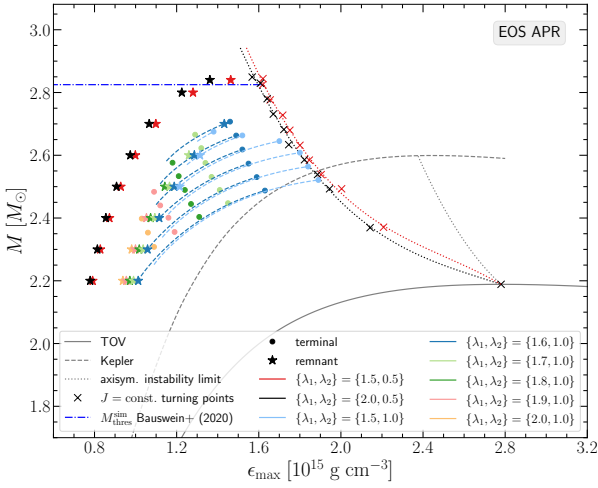


Figure 8. Gravitational mass M vs. maximum energy density ϵ_{\max} for the APR EOS. Six choices of rotation law parameters yielding Type A solutions are presented (λ_1 varies from 1.5 to 2 while λ_2 is held fixed and equal to 1). The nonrotating (TOV) sequence (grey solid line), the mass-shedding (Kepler) limit for uniform rotation (grey dashed line) and the axisymmetric instability limit for uniform rotation (grey dotted line), together with the data corresponding to Type C solutions are shown as reference.

we explicitly show the constant angular momentum sequences (as light blue and dark blue dashed lines respectively). We note that the $\{\lambda_1, \lambda_2\} = \{1.6, 1.0\}$ J -constant lines in Figure 8 nearly merge into those of $\{\lambda_1, \lambda_2\} = \{1.5, 1.0\}$ as the maximum density increases. J -constant lines constructed with other pairs of $\{\lambda_1, \lambda_2\}$ also tend to merge with those of $\{\lambda_1, \lambda_2\} = \{1.5, 1.0\}$, but for clarity, we omit the J -constant lines for $\lambda_1 = \{1.7, 1.8, 1.9, 2.0\}$ in Figure 8. Moreover, as a rule of thumb the J -constant lines for $\{\lambda_1, \lambda_2\} = \{1.5, 1.0\}$ reach higher maximum densities than the J -constant lines for $\{\lambda_1, \lambda_2\} = \{1.6, 1.0\}$. Note though, that for the highest J -constant sequence for the APR and DD2 EOS (Figures 8 and 9 respectively), this trend is reversed, i.e. it is the highest J -constant line for $\{\lambda_1, \lambda_2\} = \{1.6, 1.0\}$ that actually reaches higher maximum densities. In our investigation of this behaviour, we found that an increasingly smaller step size in axis ratio was required (reaching as low as 10^{-4}) to locate equilibrium solutions for $\{\lambda_1, \lambda_2\} = \{1.5, 1.0\}$ (which yields the weakest differential rotation we consider) in the parameter space of increasing energy density values and high angular momentum values. This effect is indicating numerical stiffness. However, one would have to perform similar trials with other equilibrium codes to clarify whether this issue: (i) has some physical origin (e.g. it could be possible that weaker differential rotation cannot produce *high enough* angular velocities to accommodate *arbitrarily high* angular momentum values), (ii) or if it is due to numerical stiffness of the problem, (iii) or if it is due to the existence of different types of differentially rotating solutions that have the same central density and axis ratio⁴.

Gathering all the evidence, some interesting observations can be made in connection to earlier works in the literature, where the KEH rotation law was used. First of all, we note that Type C remnant mod-

⁴ We note that the numerical method used in the RNS code does not discriminate between different types of models with same axis ratio, central or maximum density and differential rotation law, so that the numerical iterations can alternate between two different solutions, instead of converging to a specific one.

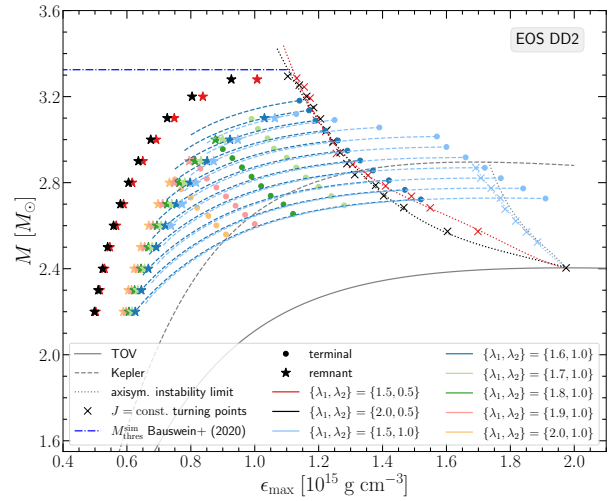


Figure 9. Same as Figure 8 for the DD2 EOS.

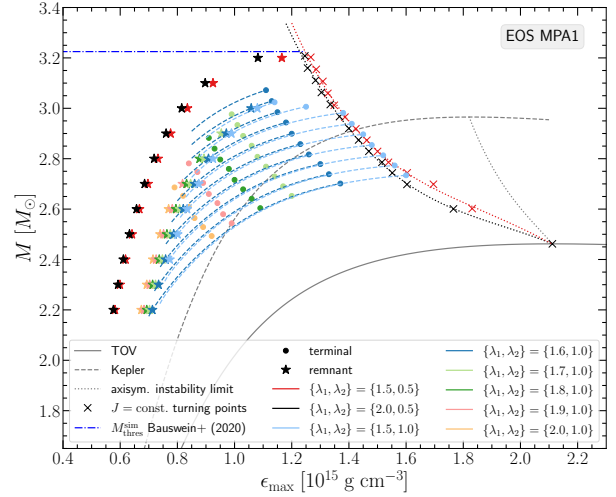


Figure 10. Same as Figure 8 for the MPA1 EOS.

els are able to reach higher masses than Type A models, in agreement with findings in Gondek-Rosińska et al. (2017); Studzińska et al. (2016); Espino & Paschalidis (2019) for the KEH rotation law. Concerning the terminal models encountered for the Type A J -constant sequences, they can be interpreted as a confirmation that the domain of Type A solutions shrinks for higher densities and stronger differential rotation. Specifically, with stronger differential rotation we do not find Type A solutions above a certain maximum energy density, whereas we can still find Type C solutions⁵ (or Type A solutions with a weak differential rotation).

The above property of differentially rotating models was highlighted for the KEH rotation law in Studzińska et al. (2016); Gondek-Rosińska et al. (2017) for polytropes, Espino & Paschalidis (2019) for realistic EOS and Szkudlarek et al. (2019) for strange quark stars. From our findings for the Uryu+ rotation law, it seems that the different types of solutions are not tied to the particular KEH rotation law

⁵ Note that we do not discuss Type B and Type D solutions of Ansorg et al. (2009) in this study. Depending on the choice of parameters, Type B solutions can co-exist with those of Type A and Type D with those of Type C.

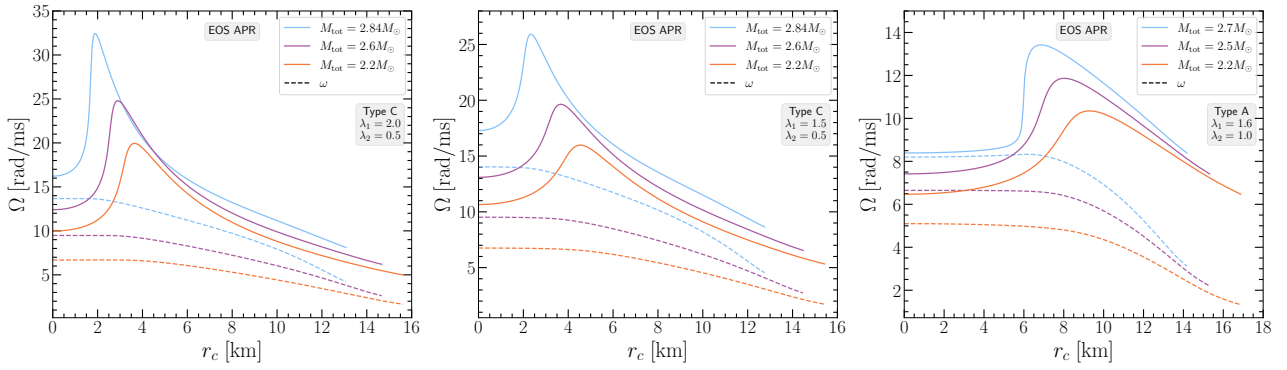


Figure 11. Angular velocity profiles Ω vs. the circumferential radial coordinate r_c , in the equatorial plane for the APR EOS. *Left panel:* Type C models with $\{\lambda_1, \lambda_2\} = \{2.0, 0.5\}$. *Middle panel:* Type C models with $\{\lambda_1, \lambda_2\} = \{1.5, 0.5\}$. *Right panel:* Type A models with $\{\lambda_1, \lambda_2\} = \{1.6, 1.0\}$. In each panel the profiles for the most massive, the least massive and an intermediate mass remnant model are shown. The dashed lines correspond to the frame dragging angular velocity $\omega(r_c)$ in the equatorial plane for each different model. For the most massive Type A model, we observe that $\Omega \approx \omega$ in the core, as has been reported in BNS merger simulations.

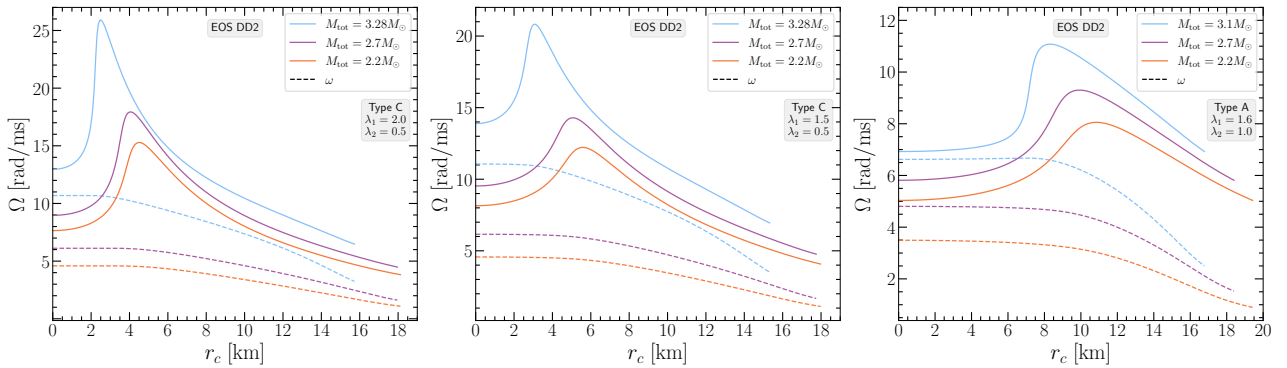


Figure 12. Same as Figure 11 for the DD2 EOS.

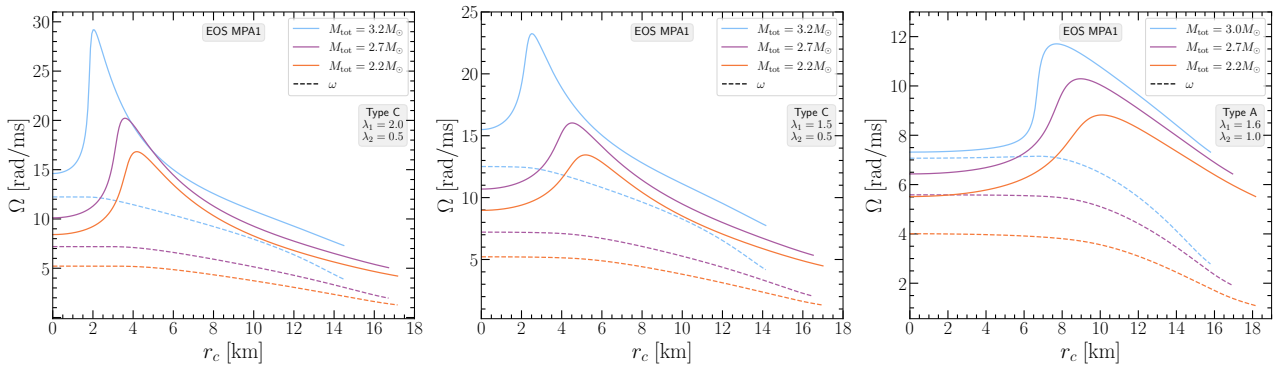


Figure 13. Same as Figure 11 for the MPA1 EOS.

(for which they were originally discovered), but appear also for other, more general rotation laws, such as the one by Uryū et al. considered here.

Figures 9 and 10 show the same investigation of Type A models as in Figure 8, but for the EOS DD2 and MPA1. We note that also for these EOS, the choice of $\lambda_1 = 1.6$ allows for the construction of the most massive Type A remnant model and also for a full remnant sequence (i.e. starting from the lowest remnant mass of $M_{\text{tot}} = 2.2M_{\odot}$ we consider). Within the parameter range that we investigated, the highest mass Type A remnant model reached with EOS DD2 was

$3.1M_{\odot}$, while for EOS MPA1 it was $3M_{\odot}$. Physical quantities of Type A remnant models are reported in Tables 5, 6 and 7 for EOS APR, DD2 and MPA1 respectively.

In Iosif & Stergioulas (2021, Figure 8) we showed that for $\{\lambda_1, \lambda_2\} = \{1.5, 1.0\}$ the differential rotation is quite weak, compared to other values of λ_1 in the range we consider here. For the stiffest EOS we consider (DD2) this leads to Type A models for which we can find turning points along the J -constant sequences (light blue dotted curve in Figure 9). Moreover, these turning points are close to the axisymmetric instability limit for uniform rotation.

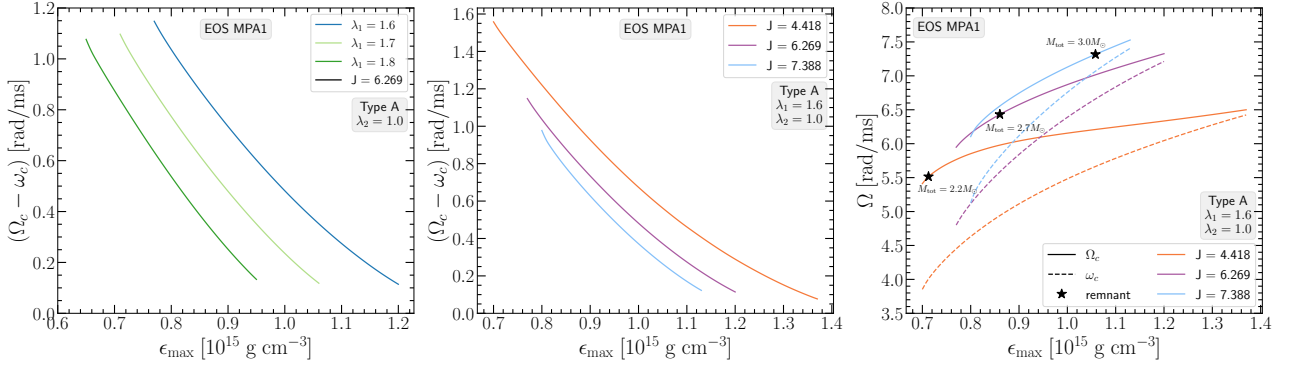


Figure 14. Investigation of the frame dragging contribution to rotation for the MPA1 EOS. *Left panel:* Difference ($\Omega_c - \omega_c$) between the angular velocity and the frame dragging values at the center of the configuration vs. the maximum energy density. The solid lines correspond to J -constant sequences with $J = 6.269$, along which remnant models with $M_{\text{tot}} = 2.7M_{\odot}$ are constructed. The colors represent different options for λ_1 yielding different strengths of differential rotation and are matching the colors of the respective options in Figure 10 for ease of reference. *Middle panel:* Same quantities plotted as in the left panel, but for a single strength of differential rotation $\{\lambda_1, \lambda_2\} = \{1.6, 1.0\}$. The solid lines are J -constant sequences corresponding to the most massive ($M_{\text{tot}} = 3.0M_{\odot}$), least massive ($M_{\text{tot}} = 2.2M_{\odot}$) and an intermediate mass $M_{\text{tot}} = 2.7M_{\odot}$ remnant model. *Right panel:* Central angular velocity Ω_c (solid lines) and frame dragging at the center ω_c (dashed lines) vs. the maximum energy density for $\{\lambda_1, \lambda_2\} = \{1.6, 1.0\}$. The different colors correspond to the same J -constant sequences as in the middle panel. The asterisks represent the respective remnant models. The colors selected in the middle and right panels match those of the right panel of Figure 13 for ease of reference.

3.3 Frame dragging contribution to rotation

Figures 11, 12 and 13 show the angular velocity $\Omega(r_c)$ rotational profiles versus the circumferential radial coordinate r_c at the equatorial plane, for the three EOS under study, APR, DD2 and MPA1. For each EOS, a triplet of panels is shown, with each left panel corresponding to rotation laws $\{\lambda_1, \lambda_2\} = \{2.0, 0.5\}$, each middle panel to $\{\lambda_1, \lambda_2\} = \{1.5, 0.5\}$ and each right panel to $\{\lambda_1, \lambda_2\} = \{1.6, 1.0\}$. Every individual panel shows $\Omega(r_c)$, as well as the frame dragging angular velocity $\omega(r_c)$ for the most massive, the least massive and for an intermediate mass remnant model constructed with the particular choice of parameters $\{\lambda_1, \lambda_2\}$. A common finding shared among the three EOS explored, is that models with $\{\lambda_1, \lambda_2\} = \{2.0, 0.5\}$ reach the highest angular velocity compared to the other two options and models with $\{\lambda_1, \lambda_2\} = \{1.6, 1.0\}$ reach the smallest angular velocity peaks in their profile. This is in agreement with corresponding rotational profiles for these parameter values for polytropic equilibrium models with $N = 1$ (Iosif & Stergioulas 2021, Figure 8).

Examining Type A remnants we observe that for the most massive models the central part of the configuration (i.e. approximately up to $r_c \sim 5$ km) rotates slowly compared to the rest of the configuration. However, this rotation rate is mostly due to the contribution of the frame dragging ω , which means that with respect to a ZAMO this part of the model is *almost nonrotating*. To our knowledge, this is the first time that a differential rotation law has been shown to reproduce this feature, already known from numerical simulations: similar rotation profiles have been presented and analyzed in Kastaun & Galeazzi (2015); Endrizzi et al. (2016); Kastaun et al. (2016, 2017); Ciolfi et al. (2017).

Note that we did not observe the $\Omega \sim \omega$ behaviour near the center of the star *only* for the most massive Type A models (i.e. the rightmost dark blue asterisks of the remnant sequences for $\{\lambda_1, \lambda_2\} = \{1.6, 1.0\}$ in Figures 8, 9 and 10 corresponding to the light blue curves of the right panels in Figures 11, 12 and 13 for each EOS considered). This feature also appears in less massive models that have higher central densities (i.e. models neighbouring the terminal models shown as dark blue dots for $\{\lambda_1, \lambda_2\} = \{1.6, 1.0\}$ in Figures 8, 9 and 10). Specifically, for *all* the rotation law parameters yielding Type A configurations that we considered (i.e. the six $\{\lambda_1, \lambda_2\}$ pairs with

$\lambda_2 = 1.0$ in Figures 8, 9 and 10), we found that ω approaches Ω as the maximum density increases along a J -constant sequence, until the $\Omega \sim \omega$ feature appears as we reach the terminal model. To clarify even further, we found that

- along a J -constant sequence, the $\Omega \sim \omega$ behaviour appears at lower central densities as the strength of differential rotation is increased⁶ (see left panel of Figure 14)
- for a specified strength of differential rotation (i.e. fixing the differential rotation law's parameters at certain values), the $\Omega \sim \omega$ behaviour appears at lower central densities as the angular momentum J is increased (see middle panel of Figure 14).
- as the maximum energy density is increased along a J -constant sequence, the frame dragging at the center ω_c *increases faster* than the central angular velocity Ω_c , thus giving rise to the $\Omega \sim \omega$ feature (see right panel of Figure 14).

Note that while Figure 14 demonstrates the above for the MPA1 EOS, similar behaviour is observed for the other two EOS that we studied.

3.4 $\Omega(F)$ profiles

Figures 15, 16 and 17 follow the same organization as corresponding figures for the rotation profiles $\Omega(r_c)$ and present the angular velocity $\Omega(F)$ profiles that define each rotation law. We find that for each choice of rotation law parameters (e.g. if one observes the left panels of Figures 15, 16 and 17 "vertically", etc.) the resulting $\Omega(F)$ profiles are qualitatively similar between the three EOS that we consider. This is in agreement with analogous behaviour of the corresponding $\Omega(r_c)$ profiles in Figures 11, 12 and 13.

Note that in all cases, the inverse profile, $F(\Omega)$, would not be a one-to-one function. In the case of the KEH rotation law, one can simply integrate $F(\Omega)$ in the equation of hydrostationary equilibrium. However, for the Uryu+ rotation law, one needs to express the

⁶ This holds as a rule of thumb, barring a possible numerical stiffness encountered for high J values and weak differential rotation (see discussion in Section 3.2).

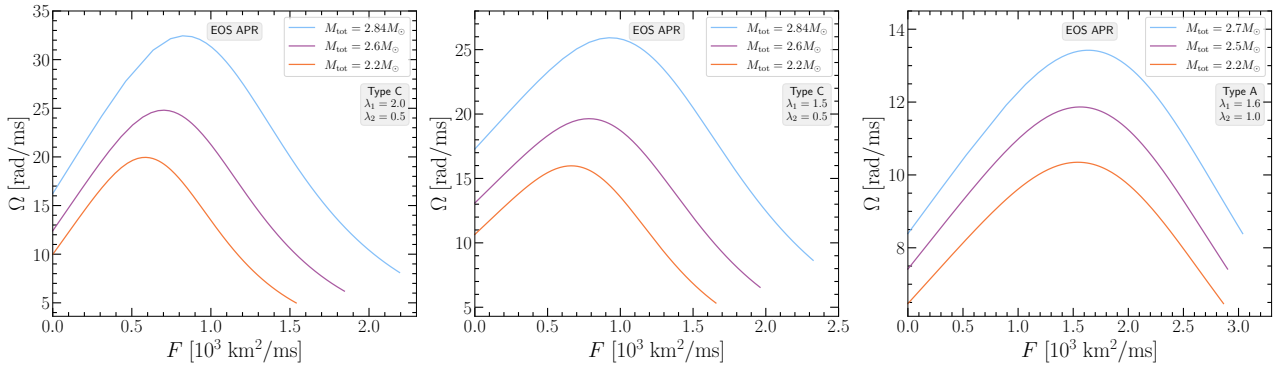


Figure 15. Angular velocity profiles Ω vs. the gravitationally redshifted angular momentum per unit rest mass and enthalpy F , in the equatorial plane for the APR EOS. *Left panel:* Type C models with $\{\lambda_1, \lambda_2\} = \{2.0, 0.5\}$. *Middle panel:* Type C models with $\{\lambda_1, \lambda_2\} = \{1.5, 0.5\}$. *Right panel:* Type A models with $\{\lambda_1, \lambda_2\} = \{1.6, 1.0\}$. In each panel the profiles for the most massive, the least massive and an intermediate mass remnant model are shown.

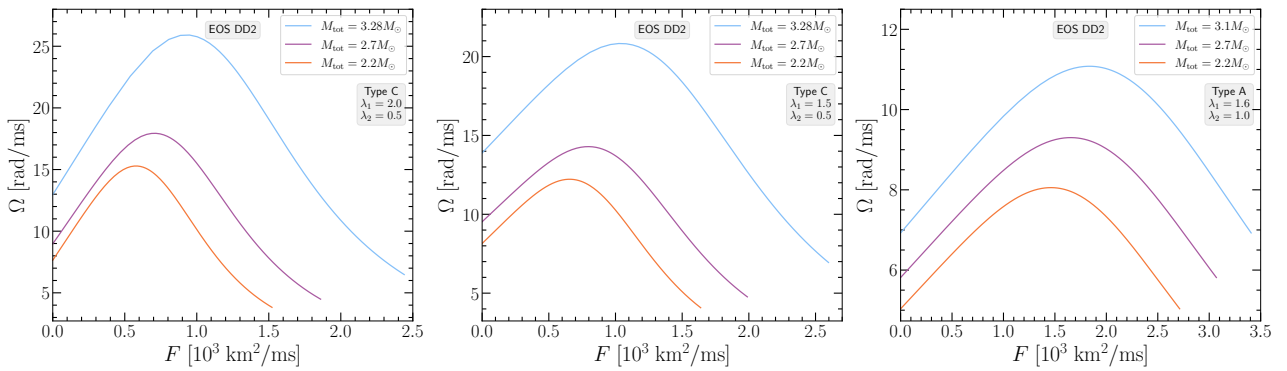


Figure 16. Same as Figure 15 for the DD2 EOS.

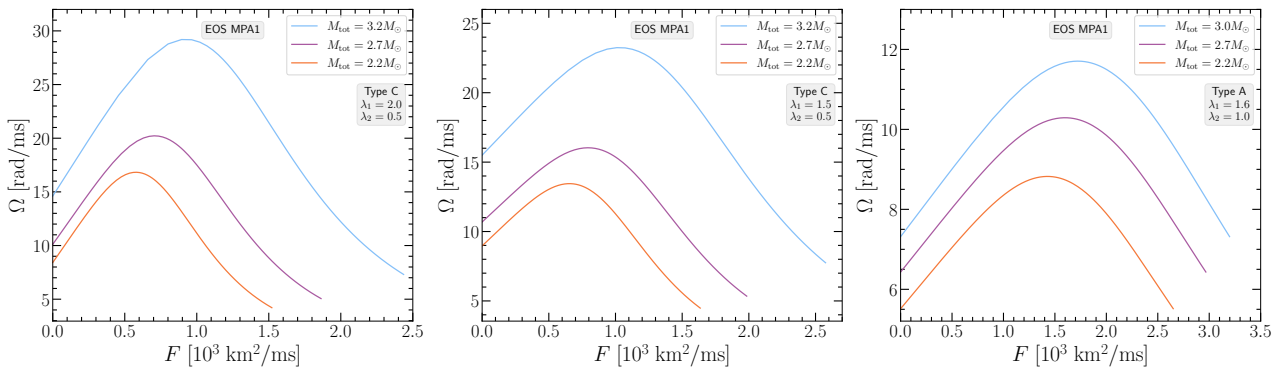


Figure 17. Same as Figure 15 for the MPA1 EOS.

equation of stationary equilibrium in terms of an integral $\Omega(F)$ (see Iosif & Stergioulas (2021) for details).

3.5 Structure of the remnants: surface and density distribution

Stellar surfaces in the $x-z$ plane (with x and z normalized with the equatorial coordinate radius r_e) for the most massive, least massive and an intermediate mass remnant model are shown in Figures 18, 19 and 20, for the three EOS employed and for three different choices of parameters $\{\lambda_1, \lambda_2\}$ (similar to the corresponding figures of the rotation profiles). We note that for tabulated EOS we always have a finite minimum pressure value P_{\min} at the minimum density ρ_{\min} .

For the three EOS employed, the range of ρ_{\min} is sub-grid varying from $\sim 8 \text{ g cm}^{-3}$ to $\sim 10^3 \text{ g cm}^{-3}$, i.e. so small that not a single grid point is removed from the model. Furthermore, since the RNS code constructs numerical tables in log enthalpy, a very small enthalpy value H_{\min} (of order 10^{-16}) is used in the tabulated EOS files. Then, the stellar surface is defined as the location where the pressure $P = P_{\min}$ and the enthalpy $H = H_{\min}$. Interpolating the model's enthalpy by demanding that its value matches H_{\min} allows to pinpoint the surface's location. In addition, Figures 21, 22 and 23 display the two-dimensional rest-mass density distributions for the most massive models in the meridional plane.

Note that the surfaces and meridional density profiles are quali-

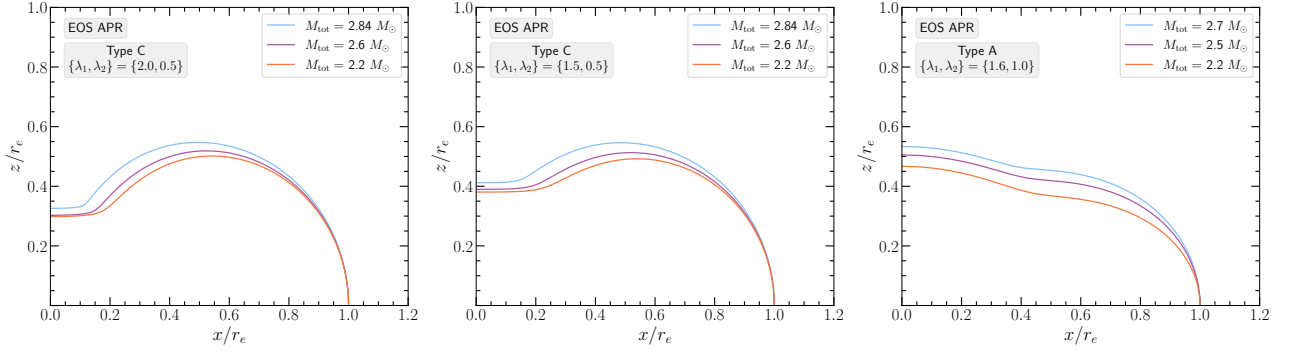


Figure 18. Stellar surfaces for the APR EOS. *Left panel:* Type C models with $\{\lambda_1, \lambda_2\} = \{2.0, 0.5\}$. *Middle panel:* Type C models with $\{\lambda_1, \lambda_2\} = \{1.5, 0.5\}$. *Right panel:* Type A models with $\{\lambda_1, \lambda_2\} = \{1.6, 1.0\}$. In each panel the surfaces of the most massive, the least massive and an intermediate mass remnant model are shown.

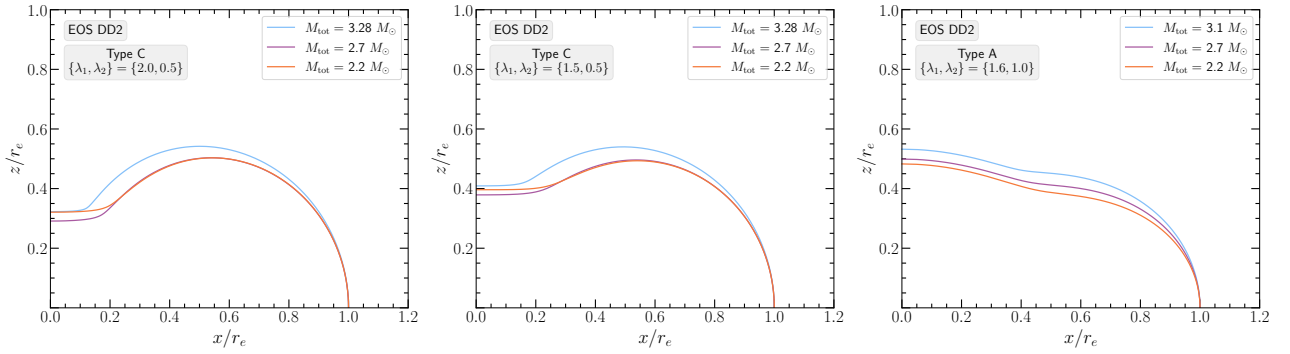


Figure 19. Same as Figure 18 for the DD2 EOS.

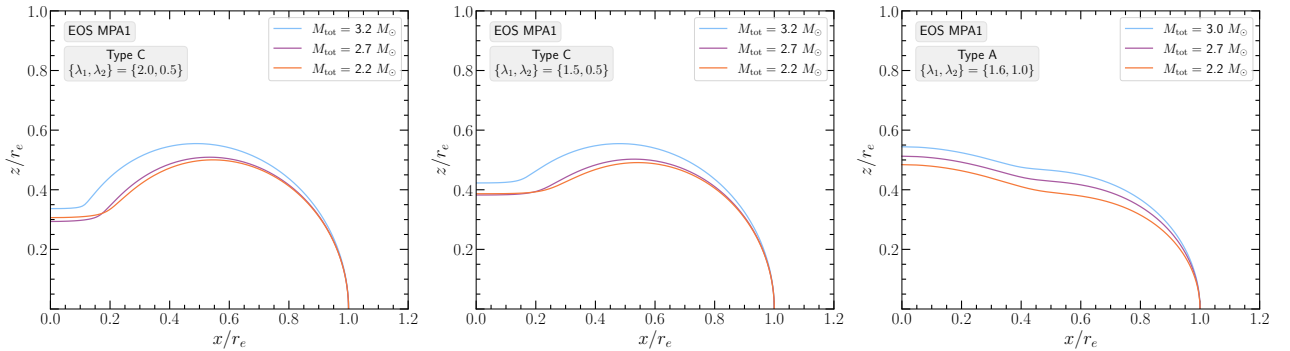


Figure 20. Same as Figure 18 for the MPA1 EOS.

tatively similar for the Type C solutions obtained with $\{\lambda_1, \lambda_2\} = \{2.0, 0.5\}$ and $\{\lambda_1, \lambda_2\} = \{1.5, 0.5\}$. Both choices lead to a quasi-toroidal surface shape, typical for Type C solutions. For $\{\lambda_1, \lambda_2\} = \{2.0, 0.5\}$, we observe a stronger deformation close to the rotation axis than for $\{\lambda_1, \lambda_2\} = \{1.5, 0.5\}$, which is explained by the stronger differential rotation.

For the Type A solutions obtained with $\{\lambda_1, \lambda_2\} = \{1.6, 1.0\}$, the surfaces of all models (most massive to least massive) are quite similar to each other (when coordinates are scaled by r_e). Even though the remnant models have significant oblateness, they still retain their quasi-spherical shape (the central density is also the maximum density). It is interesting to note that for these selected Type A remnants, the axis ratio r_p/r_e ranges between $\sim 0.47 -$

0.54 , whereas for the Type C remnants the corresponding range is considerably lower at $\sim 0.3 - 0.42$.

Recently, [Kastaun et al. \(2016\)](#) introduced a new measure that replaces density profiles, mass, and compactness in a way that can be used unambiguously for rapidly and differentially rotating merger remnants, without a clearly defined surface. Therefore, we stress that the profiles presented here serve simply as an indication about the different configurations possible for the different cold EOS employed and for the $\{\lambda_1, \lambda_2\}$ options we considered. In a realistic remnant with a hot envelope and mass-shedding, the density distribution would not terminate at the same radius as in our models and one would need to define an approximate surface shape, based e.g. on the location where the density drops to a certain fraction of the maximum density.

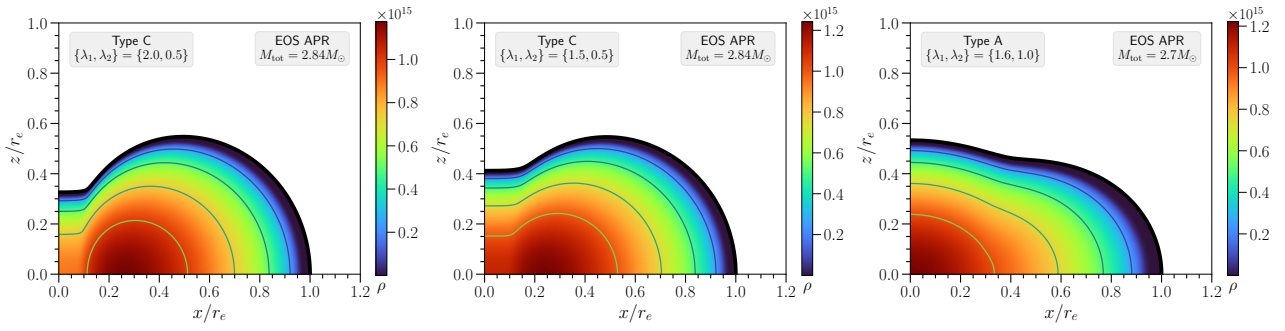


Figure 21. Two-dimensional rest mass density distribution ρ [g cm^{-3}] of the most massive remnant models for the APR EOS. *Left panel:* Type C model with $\{\lambda_1, \lambda_2\} = \{2.0, 0.5\}$. *Middle panel:* Type C model with $\{\lambda_1, \lambda_2\} = \{1.5, 0.5\}$. *Right panel:* Type A model with $\{\lambda_1, \lambda_2\} = \{1.6, 1.0\}$.

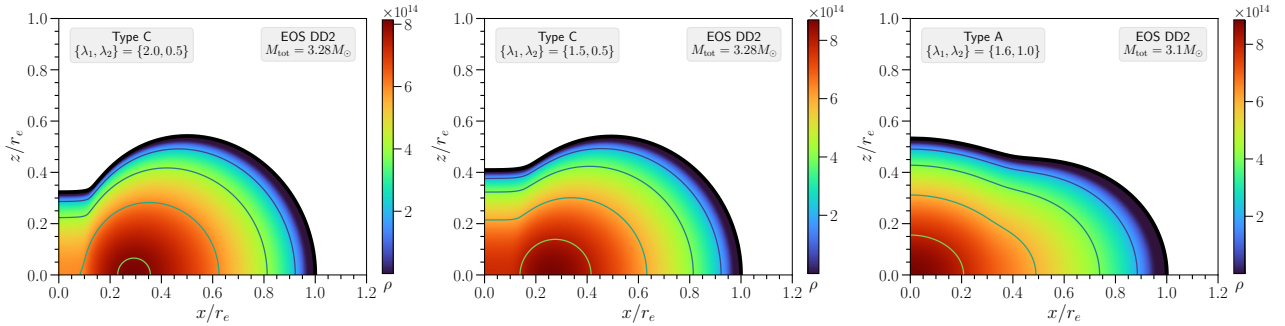


Figure 22. Same as Figure 21 for the DD2 EOS.

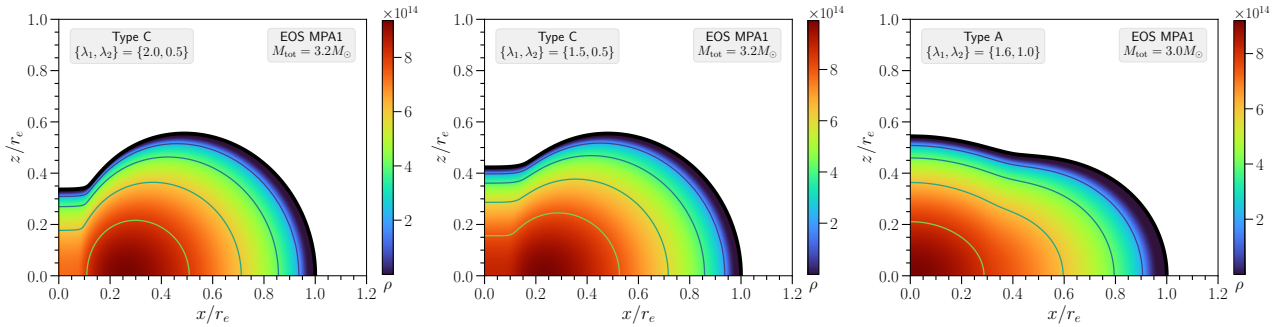


Figure 23. Same as Figure 21 for the MPA1 EOS.

3.6 Mass vs. equatorial radius

Having presented the main characteristics of our models in the previous subsections, we further analyze our findings by constructing $M(R_e)$ plots (i.e. gravitational mass versus equatorial circumferential radius) for the remnant models. We focus on the choice $\{\lambda_1, \lambda_2\} = \{2.0, 0.5\}$ that represents the strongest differential rotation we consider, but note that a similar picture holds for the case $\{\lambda_1, \lambda_2\} = \{1.5, 0.5\}$.

Figures 24, 25 and 26 show $M(R_e)$ for the EOS APR, DD2 and MPA1 respectively. In each of these figures, remnant sequences are shown as dots (denoting the equilibrium models), connected by solid interpolated lines. The dotted lines represent J -constant sequences, turning points are marked by crosses and a linear fit (dashed line) approximates the turning point sequence. The annotation in these figures means that while the empirical relation (8) by Lucca et al. (2021) provides a predicted J_{merger} value for a desired target

Table 3. Coefficients of the linear fits $M = a_1 R_e - b_1$ and their respective errors, for the turning point sequences with $\{\lambda_1, \lambda_2\} = \{2.0, 0.5\}$ of each EOS (Figures 24, 25 and 26). The errors in the coefficients of the linear fits, δa_1 and δb_1 , are calculated with the standard formulas of simple linear regression and correspond to uncertainties at the 1σ level.

EOS	a_1	b_1	δa_1	δb_1
APR	0.2769	0.5936	0.0048	0.0574
DD2	0.3077	1.2876	0.0040	0.0564
MPA1	0.2969	0.9268	0.0029	0.0382

M_{tot} , the intersection of the remnant sequence and the turning point sequence has already taken place. Therefore, the target M_{tot} model for the specific J_{merger} value predicted by (8), does not exist, since it would exceed the value of M_{thres} .

For the turning point sequences, Table 3 lists the coefficients a_1, b_1

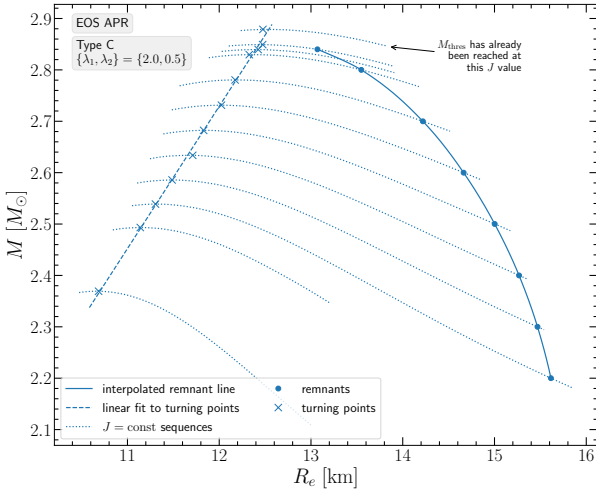


Figure 24. Gravitational mass M vs. equatorial circumferential radius R_e for models constructed with the Uryu+ rotation law, using $\{\lambda_1, \lambda_2\} = \{2.0, 0.5\}$, for the APR EOS. Each dotted line is a J -constant sequence and a cross indicates the turning point model. The dashed line is a linear fit through the turning point models. The filled circles represent the sequence of remnant models.

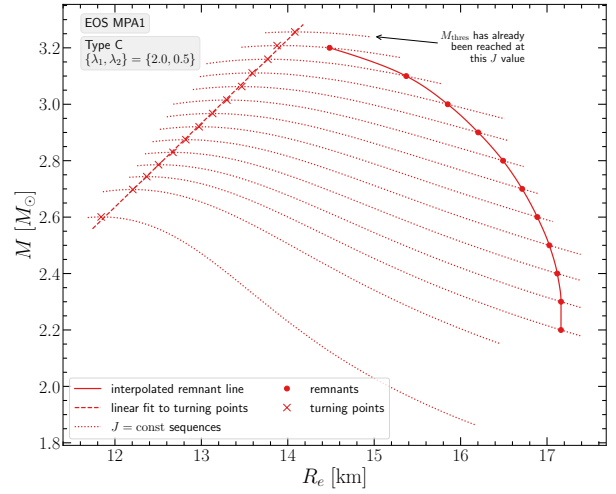


Figure 26. Same as Figure 24 for the MPA1 EOS.

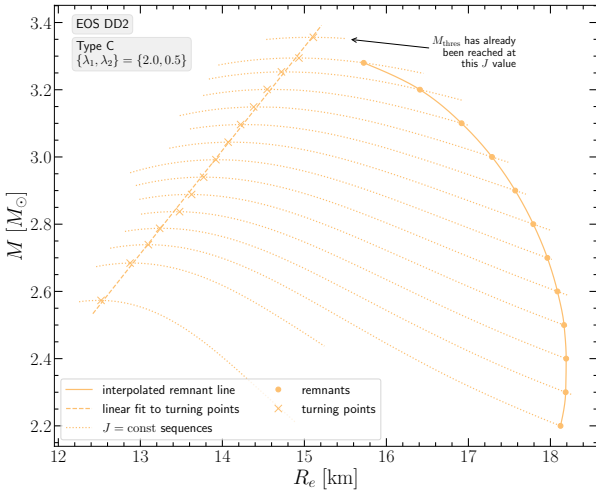


Figure 25. Same as Figure 24 for the DD2 EOS.

for a linear fit of the form

$$M = a_1 R_e - b_1, \quad (12)$$

as well as their respective errors (with uncertainties at the 1σ level). We find that the three slopes (a_1) are comparable, a fact which may be related to the universalities found by [Bozzola et al. \(2018\)](#) for turning point sequences. Only the slope of the fit for the APR EOS (the softest of the three) differs somewhat from the corresponding slope for the other two EOS. We note that the relative difference in slopes between the linear fits for the APR and DD2 EOS (the stiffest EOS we consider) is only $\sim 10\%$, which is noteworthy given that equation (12) correlates a bulk quantity (mass) with a local quantity (radius) that encodes more prominently a dependence on the EOS.

Collecting data from all EOS in a single $M(R_e)$ plot, Figure 27, one could extrapolate the remnant sequences so that they intersect with the turning point sequences and obtain the intersection $(M_{\text{thres}}, R_{e-\text{thres}})$. We note that the M_{thres} values determined in this

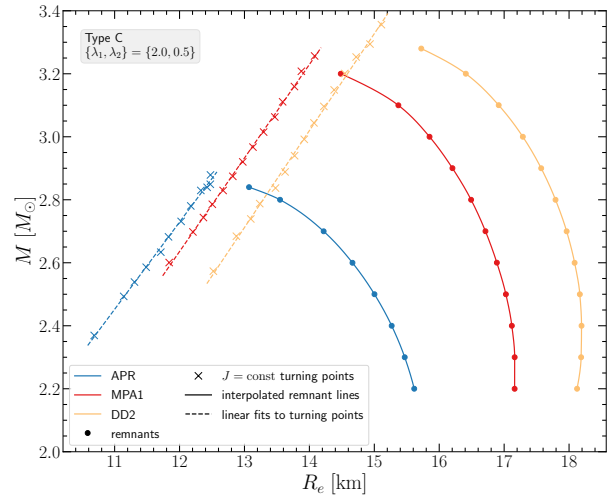


Figure 27. Same as Figure 24, showing collectively remnants and turning points for all EOS considered.

way are in good agreement with those reported in Table 2. Still, we regard the values in Table 2 as better estimates for $M_{\text{thres}}^{\text{eq}}$, since they involve bulk quantities of the star, such as the angular momentum J and the mass M , with direct input from numerical simulations, via (8), to determine J . Moreover, the precise determination of $R_{e-\text{thres}}$, in actual remnants is affected by the thermal properties of low-density material and one needs to resort to a particular definition, based on an isodensity surface, where the density has become a certain small fraction of the maximum density. The notion of a "bulk" region and the relative measure introduced in [Kastaun et al. \(2016\)](#) is relevant in this respect.

3.7 Mass vs. equatorial compactness and a criterion for prompt collapse

The almost identical slope of the turning point lines in the $M(R_e)$ plot of Figure 27, implies that the threshold mass to collapse will be attained at about the same value of the ratio M/R_e , for all three EOS considered. In correspondence to the usual definition of the

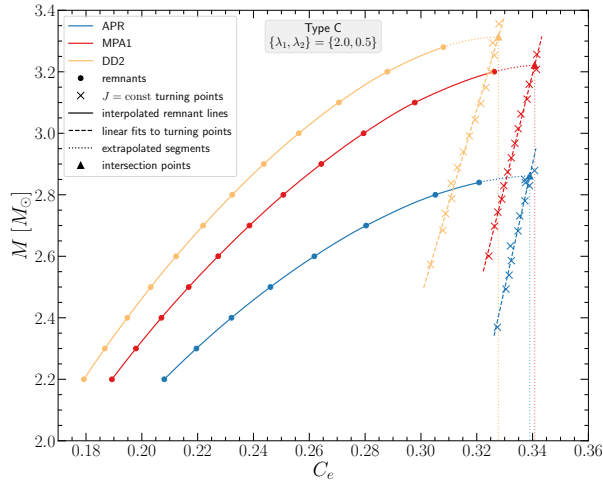


Figure 28. Gravitational mass M vs. equatorial compactness C_e for all EOS considered for the Type C models with $\{\lambda_1, \lambda_2\} = \{2.0, 0.5\}$.

compactness of a nonrotating star $C = M/R$, we define the ratio $C_e = M/R_e$ as the *equatorial compactness*.

Figure 28 displays the $M(C_e)$ relation for the remnant sequences and turning point sequences for the three EOS. The turning point sequences are practically straight lines and we list the coefficients (along with their 1σ errors) of linear fits of the form

$$M = a_2 C_e - b_2 \quad (13)$$

in Table 4. Dotted lines are extrapolations⁷ of each remnant sequence to its intersection with the corresponding turning point sequence for the same EOS. The intersection of the two sequences for each EOS marks the value $C_{e-\text{thres}}$ for the model at the threshold mass M_{thres} . These values are also listed in Table 4 along with the maximum compactness $C_{\text{max}}^{\text{TOV}}$ of stable nonrotating models, for the same EOS.

At present, we only list three data points and it is not possible to decide whether the data imply a nearly constant $C_{e-\text{thres}} \sim 1/3$ or a strong correlation between $C_{e-\text{thres}}$ and $C_{\text{max}}^{\text{TOV}}$. A linear fit of the current data yields

$$C_{e-\text{thres}} \simeq 0.48 C_{\text{max}}^{\text{TOV}} + 0.184, \quad (14)$$

but additional EOS will be required to clarify whether the equatorial compactness at the threshold mass to prompt collapse, $C_{e-\text{thres}}$, is a universal value, or whether it is strongly correlated with the maximum compactness $C_{\text{max}}^{\text{TOV}}$ of stable nonrotating models. Either way, our results imply that a criterion for prompt collapse can be formulated, using the equatorial compactness of equilibrium models of BNS remnants.

It is interesting that in simulations with the SFHo EOS by [Kastaun & Ohme \(2021\)](#) a “bulk” compactness of 0.31 for the remnant 1ms before collapse is reported, with $C_{\text{max}}^{\text{TOV}} = 0.295$ for the maximum mass TOV model for this specific EOS. In [Kastaun et al. \(2016\)](#) it was found that the core of the remnant has a mass profile that resembles that of a TOV solution, with similar findings echoed by [Ciolfi et al.](#)

⁷ The remnant sequences are interpolated using the package `PchipInterpolator` from the `SciPy` library ([Virtanen et al. 2020](#)). This package incorporates the Piecewise Cubic Hermite Interpolating Polynomial (PCHIP) algorithm ([Fritsch & Butland 1984](#)) and additionally provides an extrapolation option. The latter uses the monotonic cubic spline from the last interval of the data to find the value of the points in the extrapolated range.

Table 4. Coefficients of the linear fits $M = a_2 C - b_2$ and their respective errors, for the turning point sequences with $\{\lambda_1, \lambda_2\} = \{2.0, 0.5\}$ of each EOS (Figure 28). The errors in the coefficients of the linear fits, δa_2 and δb_2 , are calculated with the standard formulas of simple linear regression and correspond to uncertainties at the 1σ level. Values for $C_{e-\text{thres}}$ at the intersection points are also listed, together with the corresponding values for $C_{\text{max}}^{\text{TOV}}$ of the maximum mass TOV model for each EOS.

EOS	a_2	b_2	δa_2	δb_2	$C_{e-\text{thres}}$	$C_{\text{max}}^{\text{TOV}}$
APR	40.6218	10.9095	2.8194	0.9435	0.339	0.326
DD2	30.4530	6.6678	0.8999	0.2854	0.328	0.300
MPA1	36.3972	9.1811	0.7741	0.2579	0.341	0.321

(2017). The latter study went on to suggest the conjecture that merger remnants that do not admit a TOV core equivalent⁸ promptly collapse to a black hole. It will be interesting to explore these prospects with equilibrium modelling in future work, now that we have provided proof of concept that the Uryu+ law can capture the $\Omega \sim \omega$ feature in the core of remnants, as it has been observed in simulations.

4 DISCUSSION AND OUTLOOK

In this study, we followed up on our recent work ([Iosif & Stergioulas 2021](#)) and expanded our investigation of relativistic equilibrium models, using the 4-parameter differential rotation law of [Uryū et al. \(2017\)](#) and cold, tabulated EOS of high-density matter. We constructed sequences of merger remnants, taking advantage of empirical relations for the angular momentum at merger, derived through numerical simulations. Comparing the rotational profiles $\Omega(r_c)$, the $\Omega(F)$ profiles, the stellar surfaces and the meridional rest mass density profiles of our remnant models between the three EOS we employed, we found that all respective profiles studied are qualitatively similar when the rotation law parameters are held fixed to different values. Furthermore, choices for the rotation law parameters that yield the *same* Type of solutions (i.e. either Type A or C) also show qualitative similarities in profiles even when varying the parameter λ_1 .

In addition, we constructed constant angular momentum sequences. From the intersection of the line connecting the turning points of J -constant sequences and the merger remnant sequence, we were able to reproduce the threshold mass to prompt collapse, M_{thres} with a relative difference of only $\sim 1\%$, compared to accurate binary neutron star merger simulations. We stress that this was achieved using the same rotation law, i.e. the same values for the rotation law parameters $\{\lambda_1, \lambda_2\}$ for all three EOS used in this study.

Our investigation of the threshold mass to collapse, using equilibrium models, also points towards a possible connection between the equatorial compactness $C_e = M/R_e$ at the threshold and the maximum compactness of nonrotating models $C_{\text{max}}^{\text{TOV}}$. This lends support to the conjecture by [Ciolfi et al. \(2017\)](#), that merger remnants collapse if their relatively cold and slowly rotating inner region does not admit a stable TOV equivalent.

Another key prediction of binary neutron star merger simulations

⁸ The TOV core equivalent, is defined as the “bulk” of a TOV star, meaning the region enclosed by the isodensity surface with the maximum compactness $C_V = M_b/R_V$, where V is the total enclosed proper 3-volume by the isodensity surface, M_b is the respective total baryon mass and R_V is a volumetric radius defined through $V = \frac{4}{3}\pi R_V^3$. See [Kastaun et al. \(2016\)](#) for further details.

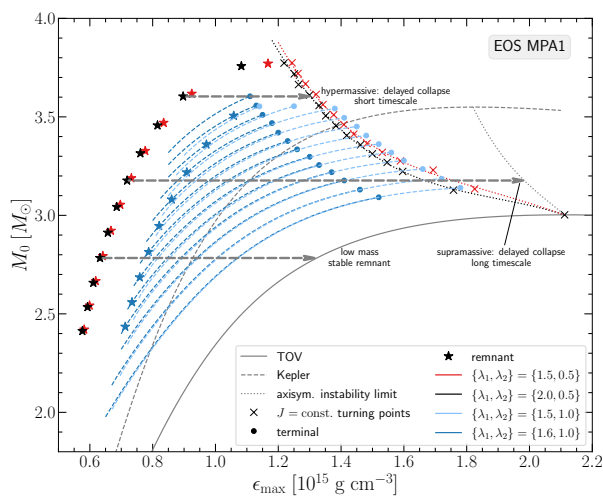


Figure 29. Rest mass M_0 vs. maximum energy density ϵ_{\max} for the MPA1 EOS. The different sequences are as in Fig. 10. The grey dashed arrows indicate possible evolutionary paths of merger remnants as they lose angular momentum, if mass loss is neglected.

is a relatively slowly rotating inner region, where the angular velocity Ω (as measured by an observer at infinity) is mostly due to the frame dragging angular velocity ω . In our investigation of the parameter space of the Uryu+ rotation law, we naturally find quasi-spherical (Type A) remnant models with this property. Both the density distribution and the angular velocity profile of these models have striking similarities with merger remnants produced in simulations (except for the low-density regions, since we neglect thermal effects).

In a forthcoming study, we plan to take the next step in this program and construct equilibrium models with finite-temperature EOS, using temperature and electron fraction profiles extracted from simulations of BNS mergers. This should allow us to isolate the effect of the thermal state of the remnant on the key properties that we discuss above. Based on Kaplan et al. (2014); Camelió et al. (2019, 2021); Chakravarti & Andersson (2020) we do not expect dramatic deviations for bulk properties of the remnants (such as their mass and angular momentum) when thermal effects are included, whereas the corresponding angular velocity profiles could exhibit a larger effect depending on the different thermal treatments (Raithel et al. 2021). One can still expect an increased radius, due to the added thermal support (see e.g. Koliogiannis & Moustakidis 2021), and consequences on longer timescales, such as convective instabilities.

In our study, we construct models of merger remnants that have angular momentum equal to the angular momentum at the time of merger, as extracted from simulations. Due to the excitation of non-axisymmetric oscillations in the remnant (as well as non-axisymmetric features, such as spiral arms), the GW emission in the post-merger phase will result in a reduction of the angular momentum with time. The remnant’s evolutionary path due to various dissipative processes taking place, could be tracked by constructing evolutionary sequences of equilibrium models. To a first approximation, one could neglect mass losses and construct evolutionary sequences keeping the rest mass of the remnant, M_0 , fixed in time.

With this viewpoint and following the related discussion in Kaplan et al. (2014), we show in Figure 29 the rest mass M_0 versus the maximum energy density ϵ_{\max} for the MPA1 EOS and the rotation law with $\{\lambda_1, \lambda_2\} = \{1.6, 1.0\}$. Analogously to Figure 10, the blue dashed lines represent constant angular momentum sequences, with sequences for $J = \{3.0, 3.5, 4.0\}$ as well as those reported in Table 7.

We note that no remnant models are located for these lower J -constant sequences, since their lower masses (implying a binary total mass $M_{\text{tot}} < 2.2M_{\odot}$) would make them irrelevant for this study. The arrows in Figure 29 approximate the evolutionary path of remnants as they lose angular momentum (assuming constant rest mass). A remnant will evolve towards larger densities and higher compactness, as its angular momentum decreases. In addition, the rotation law may also evolve in time. Three representative evolutionary paths are shown, resulting in a delayed collapse to a black hole on a short timescale (when the remnant is hypermassive); a delayed collapse on a longer timescale (when the remnant is supramassive and can still exist as a uniformly rotating model); and a stable remnant (when its mass is smaller than the maximum mass for nonrotating models).

The description of post-merger remnants as quasi-equilibrium models has applications in the interpretation of the post-merger GW spectrum; in the study of the threshold mass to prompt collapse; in the construction of universal or empirical relations between properties of the remnants and properties of nonrotating models; and in modeling of processes taking place on longer timescales that are relevant for multi-messenger follow-up studies of GW detections (Ciolfi et al. 2021; Rosati et al. 2021). We plan to elaborate further on these aspects in future work.

ACKNOWLEDGEMENTS

We thank Andreas Bauswein, John Friedman, Dimitrios Papadopoulos and Christos Tsagas for helpful discussions and comments. We also thank the anonymous referee for providing useful comments that improved the final manuscript. PI gratefully acknowledges support by a Virgo-EGO Scientific Forum (VESF) PhD fellowship. NS acknowledges support by the COST actions CA16214 “PHAROS”, CA16104 “GWVerse” and CA18108 “QG-MM”. The authors gratefully acknowledge the Italian Istituto Nazionale di Fisica Nucleare (INFN), the French Centre National de la Recherche Scientifique (CNRS) and the Netherlands Organization for Scientific Research, for the construction and operation of the Virgo detector and the creation and support of the EGO consortium.

DATA AVAILABILITY

The data underlying this article are available in the article.

REFERENCES

- Abbott B. P., et al., 2017a, *Phys. Rev. Lett.*, 119, 161101
- Abbott B. P., et al., 2017b, *ApJ*, 848, L12
- Abbott B. P., et al., 2017c, *ApJL*, 848, L13
- Abbott B. P., et al., 2017d, *Astrophys. J. Lett.*, 851, L16
- Abbott B. P., et al., 2018, *Phys. Rev. Lett.*, 121, 161101
- Abbott B. P., et al., 2019, *Phys. Rev. X*, 9, 011001
- Abbott B. P., et al., 2020a, *Living Rev. Relativ.*, 23, 3
- Abbott B. P., et al., 2020b, *ApJL*, 892, L3
- Ackley K., et al., 2020, *Publ. Astron. Soc. Aust.*, 37, e047
- Aggarwal N., et al., 2021, *Living Rev. Relativ.*, 24, 4
- Akmal A., Pandharipande V. R., Ravenhall D. G., 1998, *Phys. Rev. C*, 58, 1804
- Ansorg M., Gondek-Rosińska D., Villain L., 2009, *MNRAS*, 396, 2359
- Antoniadis J., et al., 2013, *Science*, 340, 448
- Bauswein A., Janka H. T., 2012, *Phys. Rev. Lett.*, 108, 011101
- Bauswein A., Stergioulas N., 2015, *Phys. Rev. D*, 91, 124056
- Bauswein A., Stergioulas N., 2017, *MNRAS*, 471, 4956

Table 5. Physical quantities for equilibrium remnant models constructed with the APR EOS and different choices of rotation law parameters. The columns show the polar to equatorial axis ratio r_p/r_e , the central energy density ϵ_c , the maximum energy density ϵ_{\max} , the gravitational mass M , the rest mass M_0 , the angular momentum J , the ratio of the rotational kinetic energy T over the absolute value of the gravitational binding energy $|W|$, the angular velocity at the rotation axis Ω_c , the maximum value of angular velocity Ω_{\max} , the angular velocity at the equator Ω_e , the angular velocity of a free particle in circular orbit at the equator Ω_K , the circumferential radius R_e , the coordinate radius r_e at the equator and the 3-dimensional general relativistic virial index GRV3.

r_p/r_e	$\epsilon_c (\times 10^{15})$	$\epsilon_{\max} (\times 10^{15})$	M	M_0	J	$T/ W $	Ω_c	Ω_{\max}	Ω_e	Ω_K	R_e	r_e	GRV3
$\{\lambda_1, \lambda_2\}$	$[\text{g cm}^{-3}]$	$[\text{g cm}^{-3}]$	$[M_\odot]$	$[M_\odot]$	$[\frac{GM_\odot^2}{c}]$		$[\text{rad/ms}]$	$[\text{rad/ms}]$	$[\text{rad/ms}]$	$[\text{rad/ms}]$	$[\text{km}]$	$[\text{km}]$	$(\times 10^{-5})$
{2.0, 0.5}													
0.2981	0.543	0.7788	2.20	2.4297	4.3365	0.2253	9.9765	19.9530	4.9882	9.1037	15.6150	11.8159	7.6519
0.2952	0.563	0.8138	2.30	2.5558	4.6733	0.2258	10.4436	20.8873	5.2218	9.4001	15.4686	11.4730	6.4827
0.2950	0.592	0.8556	2.40	2.6847	5.0105	0.2257	10.9829	21.9658	5.4914	9.7420	15.2677	11.0720	7.6786
0.2976	0.632	0.9074	2.50	2.8175	5.3469	0.2250	11.6224	23.2451	5.8112	10.1461	15.0024	10.6012	6.8382
0.3027	0.685	0.9736	2.60	2.9540	5.6820	0.2239	12.4015	24.8030	6.2007	10.6314	14.6637	10.0506	6.3562
0.3100	0.758	1.0659	2.70	3.0956	6.0176	0.2223	13.4186	26.8376	6.7093	11.2489	14.2197	9.3826	7.4427
0.3204	0.879	1.2256	2.80	3.2440	6.3517	0.2203	15.0118	30.0244	7.5059	12.1789	13.5483	8.4607	8.7865
0.3261	0.976	1.3619	2.84	3.3058	6.4839	0.2194	16.2264	32.4557	8.1132	12.8548	13.0703	7.8583	7.9165
{1.5, 0.5}													
0.3806	0.720	0.7911	2.20	2.4383	4.3365	0.2229	10.6528	15.9793	5.3264	9.2112	15.4348	11.6363	7.8407
0.3795	0.748	0.8280	2.30	2.5648	4.6734	0.2233	11.1264	16.6896	5.5632	9.5197	15.2823	11.2862	6.3160
0.3807	0.784	0.8722	2.40	2.6946	5.0105	0.2231	11.6700	17.5050	5.8350	9.8752	15.0766	10.8789	7.9935
0.3843	0.831	0.9276	2.50	2.8286	5.3469	0.2221	12.3134	18.4701	6.1567	10.2962	14.8070	10.4015	7.1972
0.3897	0.892	0.9985	2.60	2.9658	5.6820	0.2206	13.0935	19.6402	6.5467	10.7975	14.4685	9.8486	7.1570
0.3970	0.978	1.0986	2.70	3.1081	6.0175	0.2187	14.1200	21.1800	7.0600	11.4392	14.0226	9.1754	7.4033
0.4067	1.130	1.2790	2.80	3.2566	6.3517	0.2165	15.7837	23.6757	7.8919	12.4311	13.3304	8.2262	8.4743
0.4119	1.281	1.4642	2.84	3.3179	6.4839	0.2156	17.2826	25.9241	8.6413	13.2718	12.7567	7.5147	9.6980
{1.6, 1.0}													
0.4669	1.0128	1.0128	2.20	2.4567	4.3365	0.2052	6.4676	10.3482	6.4676	7.9280	16.8809	13.1466	9.4359
0.4813	1.0583	1.0583	2.30	2.5862	4.6733	0.2056	6.7609	10.8175	6.7609	8.5470	16.2804	12.3306	9.2157
0.4930	1.1154	1.1154	2.40	2.7188	5.0105	0.2051	7.0683	11.3092	7.0683	9.1070	15.7973	11.6330	9.5772
0.5051	1.1883	1.1883	2.50	2.8551	5.3468	0.2038	7.4161	11.8658	7.4161	9.6956	15.3167	10.9335	9.8606
0.5185	1.2862	1.2862	2.60	2.9961	5.6820	0.2018	7.8342	12.5347	7.8342	10.3614	14.7943	10.1838	11.8614
0.5334	1.4320	1.4320	2.70	3.1421	6.0175	0.1996	8.3892	13.4227	8.3892	11.1812	14.1770	9.3242	12.3628

- Bauswein A., Stergioulas N., 2019, *J. Phys. G: Nucl. Part. Phys.*, **46**, 113002
- Bauswein A., Janka H. T., Hebeler K., Schwenk A., 2012, *Phys. Rev. D*, **86**, 063001
- Bauswein A., Stergioulas N., Janka H.-T., 2016, *Eur. Phys. J. A*, **52**, 56
- Bauswein A., Just O., Janka H.-T., Stergioulas N., 2017, *ApJ*, **850**, L34
- Bauswein A., et al., 2020, *Phys. Rev. Lett.*, **125**, 141103
- Baym G., Pethick C., Sutherland P., 1971, *ApJ*, **170**, 299
- Bernuzzi S., 2020, *Gen. Relativ. Gravit.*, **52**, 108
- Bernuzzi S., Dietrich T., Tichy W., Brügmann B., 2014, *Phys. Rev. D*, **89**, 104021
- Bose S., Chakravarti K., Rezzolla L., Sathyaprakash B. S., Takami K., 2018, *Phys. Rev. Lett.*, **120**, 031102
- Bozzola G., Stergioulas N., Bauswein A., 2018, *MNRAS*, **474**, 3557
- Breschi M., Bernuzzi S., Zappa F., Agathos M., Perego A., Radice D., Nagar A., 2019, *Phys. Rev. D*, **100**, 104029
- Breschi M., Perego A., Bernuzzi S., Del Pozzo W., Nedora V., Radice D., Vescovi D., 2021, *MNRAS*, **505**, 1661
- Camelio G., Dietrich T., Marques M., Rosswog S., 2019, *Phys. Rev. D*, **100**, 123001
- Camelio G., Dietrich T., Rosswog S., Haskell B., 2021, *Phys. Rev. D*, **103**, 063014
- Capano C. D., et al., 2020, *Nat. Astron.*, **4**, 625
- Chakravarti K., Andersson N., 2020, *MNRAS*, **497**, 5480
- Chatzioannou K., 2020, *Gen. Relativ. Gravit.*, **52**, 109
- Chatzioannou K., Clark J. A., Bauswein A., Millhouse M., Littenberg T. B., Cornish N., 2017, *Phys. Rev. D*, **96**, 124035
- Cioffi R., 2020, *Gen. Relativ. Gravit.*, **52**, 59
- Cioffi R., Kastaun W., Giacomazzo B., Endrizzi A., Siegel D. M., Perna R., 2017, *Phys. Rev. D*, **95**, 063016
- Cioffi R., Kastaun W., Kalinani J. V., Giacomazzo B., 2019, *Phys. Rev. D*, **100**, 023005
- Cioffi R., et al., 2021, *Exp. Astron.*,
- Clark J., Bauswein A., Cadonati L., Janka H. T., Pankow C., Stergioulas N., 2014, *Phys. Rev. D*, **90**, 062004
- Clark J. A., Bauswein A., Stergioulas N., Shoemaker D., 2016, *Class. Quantum Gravity*, **33**, 085003
- Cook G. B., Shapiro S. L., Teukolsky S. A., 1992, *ApJ*, **398**, 203
- Cromartie H. T., et al., 2020, *Nat. Astron.*, **4**, 72
- De Pietri R., Feo A., Maione F., Löffler F., 2016, *Phys. Rev. D*, **93**, 064047
- De Pietri R., Feo A., Font J. A., Löffler F., Pasquali M., Stergioulas N., 2020, *Phys. Rev. D*, **101**, 064052
- De S., Finstad D., Lattimer J. M., Brown D. A., Berger E., Biwer C. M., 2018, *Phys. Rev. Lett.*, **121**, 091102
- Demorest P. B., Pennucci T., Ransom S. M., Roberts M. S. E., Hessels J. W. T., 2010, *Nature*, **467**, 1081
- Dietrich T., Bernuzzi S., Ujevic M., Brügmann B., 2015, *Phys. Rev. D*, **91**, 124041
- Dietrich T., Coughlin M. W., Pang P. T. H., Bulla M., Heinzl J., Issa L., Tews I., Antier S., 2020, *Science*, **370**, 1450
- Dietrich T., Hinderer T., Samajdar A., 2021, *Gen. Relativ. Gravit.*, **53**, 27
- Douchin F., Haensel P., 2001, *A&A*, **380**, 151
- East W. E., Paschalidis V., Pretorius F., Shapiro S. L., 2016, *Phys. Rev. D*, **93**, 024011
- East W. E., Paschalidis V., Pretorius F., Tsokaros A., 2019, *Phys. Rev. D*, **100**, 124042
- Easter P. J., Lasky P. D., Casey A. R., Rezzolla L., Takami K., 2019, *Phys. Rev. D*, **100**, 043005
- Easter P. J., Ghonge S., Lasky P. D., Casey A. R., Clark J. A., Hernandez Vivanco F., Chatzioannou K., 2020, *Phys. Rev. D*, **102**, 043011
- Endrizzi A., Cioffi R., Giacomazzo B., Kastaun W., Kawamura T., 2016, *Class. Quantum Gravity*, **33**, 164001
- Endrizzi A., Logoteta D., Giacomazzo B., Bombaci I., Kastaun W., Cioffi R.,

Table 6. Physical quantities for equilibrium remnant models constructed with the DD2 EOS and different choices of rotation law parameters. The different quantities are defined as in Table 5.

r_p/r_e	$\epsilon_c (\times 10^{15})$	$\epsilon_{\max} (\times 10^{15})$	M	M_0	J	$T/ W $	Ω_c	Ω_{\max}	Ω_e	Ω_K	R_e	r_e	GRV3
$\{\lambda_1, \lambda_2\}$	$[\text{g cm}^{-3}]$	$[\text{g cm}^{-3}]$	$[M_\odot]$	$[M_\odot]$	$[\frac{GM_\odot^2}{c}]$		$[\text{rad/ms}]$	$[\text{rad/ms}]$	$[\text{rad/ms}]$	$[\text{rad/ms}]$	$[\text{km}]$	$[\text{km}]$	$(\times 10^{-5})$
{2.0, 0.5}													
0.3208	0.3812	0.4983	2.20	2.4009	4.4513	0.2172	7.6442	15.2884	3.8221	7.3691	18.1234	14.3799	8.3706
0.3094	0.3789	0.5101	2.30	2.5198	4.8401	0.2198	7.8595	15.7190	3.9298	7.4853	18.1858	14.2529	6.9913
0.3015	0.3807	0.5240	2.40	2.6406	5.2273	0.2215	8.0980	16.1960	4.0490	7.6254	18.1922	14.0690	7.7354
0.2952	0.3847	0.5396	2.50	2.7630	5.6204	0.2228	8.3557	16.7114	4.1778	7.7787	18.1660	13.8509	10.1183
0.2921	0.3935	0.5581	2.60	2.8877	6.0109	0.2234	8.6459	17.2919	4.3230	7.9591	18.0857	13.5768	6.9961
0.2911	0.4060	0.5795	2.70	3.0146	6.4027	0.2236	8.9700	17.9401	4.4850	8.1617	17.9628	13.2582	6.9080
0.2922	0.4230	0.6051	2.80	3.1443	6.7954	0.2234	9.3389	18.6779	4.6694	8.3936	17.7916	12.8879	7.8284
0.2952	0.4447	0.6359	2.90	3.2768	7.1887	0.2229	9.7627	19.5254	4.8813	8.6588	17.5710	12.4645	6.3214
0.2999	0.4726	0.6745	3.00	3.4125	7.5817	0.2220	10.2658	20.5315	5.1329	8.9707	17.2880	11.9735	6.1169
0.3065	0.5100	0.7266	3.10	3.5524	7.9741	0.2209	10.8964	21.7932	5.4482	9.3560	16.9163	11.3854	7.7065
0.3145	0.5630	0.8044	3.20	3.6962	8.3673	0.2196	11.7581	23.5171	5.8791	9.8656	16.4095	10.6486	7.2057
0.3226	0.6410	0.9276	3.28	3.8156	8.6800	0.2188	12.9607	25.9233	6.4803	10.5450	15.7235	9.7506	7.2275
{1.5, 0.5}													
0.3962	0.4716	0.5025	2.20	2.4074	4.4513	0.2142	8.1481	12.2221	4.0740	7.4195	17.9799	14.2399	7.0193
0.3884	0.4773	0.5151	2.30	2.5270	4.8401	0.2171	8.3792	12.5687	4.1896	7.5467	18.0227	14.0929	8.6483
0.3833	0.4860	0.5299	2.40	2.6485	5.2272	0.2190	8.6292	12.9438	4.3146	7.6968	18.0142	13.8936	7.0557
0.3799	0.4970	0.5468	2.50	2.7723	5.6203	0.2203	8.9002	13.3503	4.4501	7.8635	17.9698	13.6556	8.5267
0.3784	0.5110	0.5663	2.60	2.8973	6.0109	0.2209	9.1956	13.7934	4.5978	8.0505	17.8832	13.3750	9.3444
0.3789	0.5290	0.5895	2.70	3.0256	6.4027	0.2210	9.5275	14.2913	4.7638	8.2655	17.7494	13.0433	6.7115
0.3808	0.5510	0.6168	2.80	3.1562	6.7955	0.2206	9.9002	14.8504	4.9501	8.5067	17.5734	12.6666	7.3657
0.3839	0.5778	0.6495	2.90	3.2889	7.1888	0.2199	10.3245	15.4868	5.1623	8.7788	17.3533	12.2428	7.5190
0.3887	0.6130	0.6916	3.00	3.4258	7.5817	0.2188	10.8354	16.2531	5.4177	9.1050	17.0641	11.7429	6.8216
0.3946	0.6600	0.7482	3.10	3.5656	7.9741	0.2176	11.4737	17.2106	5.7369	9.5030	16.6920	11.1526	7.5437
0.4020	0.7330	0.8376	3.20	3.7105	8.3673	0.2161	12.3874	18.5812	6.1937	10.0535	16.1580	10.3829	7.4784
0.4090	0.8670	1.0083	3.28	3.8301	8.6800	0.2155	13.8873	20.8311	6.9437	10.9019	15.3236	9.3187	8.2883
{1.6, 1.0}													
0.4828	0.6261	0.6261	2.20	2.4207	4.4513	0.1992	5.0343	8.0549	5.0343	6.5162	19.4227	15.7321	8.5887
0.4829	0.6451	0.6451	2.30	2.5421	4.8400	0.2019	5.1666	8.2666	5.1666	6.7141	19.3079	15.4256	9.8640
0.4854	0.6669	0.6670	2.40	2.6658	5.2273	0.2034	5.3104	8.4966	5.3104	6.9468	19.1243	15.0469	8.9839
0.4885	0.6916	0.6916	2.50	2.7912	5.6203	0.2045	5.4627	8.7404	5.4627	7.1879	18.9252	14.6504	10.0100
0.4933	0.7209	0.7209	2.60	2.9192	6.0109	0.2048	5.6300	9.0080	5.6300	7.4581	18.6776	14.2023	8.8487
0.4990	0.7556	0.7556	2.70	3.0495	6.4027	0.2045	5.8134	9.3014	5.8134	7.7484	18.4016	13.7228	9.1569
0.5058	0.7978	0.7978	2.80	3.1827	6.7953	0.2037	6.0192	9.6308	6.0192	8.0671	18.0894	13.2030	10.1405
0.5134	0.8510	0.8510	2.90	3.3189	7.1888	0.2026	6.2561	10.0098	6.2561	8.4222	17.7347	12.6358	9.5439
0.5222	0.9226	0.9226	3.00	3.4589	7.5818	0.2010	6.5434	10.4695	6.5434	8.8369	17.3132	11.9945	10.9882
0.5322	1.0304	1.0304	3.10	3.6029	7.9740	0.1992	6.9248	11.0797	6.9248	9.3564	16.7807	11.2302	11.8057

- 2018, *Phys. Rev. D*, **98**, 043015
- Espino P. L., Paschalidis V., 2019, *Phys. Rev. D*, **99**, 083017
- Espino P. L., Paschalidis V., Baumgarte T. W., Shapiro S. L., 2019, *Phys. Rev. D*, **100**, 043014
- Fatoyev F. J., Piekarewicz J., Horowitz C. J., 2018, *Phys. Rev. Lett.*, **120**, 172702
- Friedman J. L., Stergioulas N., 2013, *Rotating Relativistic Stars*. Cambridge Monographs on Mathematical Physics, Cambridge University Press, doi:10.1017/CBO9780511977596
- Friedman J. L., Stergioulas N., 2020, *Int. J. Mod. Phys. D*, **29**, 2041015
- Friedman J. L., Ipser J. R., Sorkin R. D., 1988, *ApJ*, **325**, 722
- Fritsch F. N., Butland J., 1984, *SIAM J. Sci. and Stat. Comput.*, **5**, 300
- Galeazzi F., Yoshida S., Eriguchi Y., 2012, *A&A*, **541**, A156
- Ganapathy D., McCuller L., Rollins J. G., Hall E. D., Barsotti L., Evans M., 2021, *Phys. Rev. D*, **103**, 022002
- Gendreau K. C., et al., 2016, in den Herder J.-W. A., Takahashi T., Bautz M., eds, *Society of Photo-Optical Instrumentation Engineers (SPIE) Conference Series Vol. 9905, Space Telescopes and Instrumentation 2016: Ultraviolet to Gamma Ray*. p. 99051H, doi:10.1117/12.2231304
- Goldstein A., et al., 2017, *ApJL*, **848**, L14
- Gondek-Rosińska D., Kowalska I., Villain L., Ansorg M., Kucaba M., 2017, *ApJ*, **837**, 58
- Hall E. D., Evans M., 2019, *Class. Quantum Gravity*, **36**, 225002
- Hanauske M., Takami K., Bovard L., Rezzolla L., Font J. A., Galeazzi F., Stöcker H., 2017, *Phys. Rev. D*, **96**, 043004
- Haster C.-J., Chatziioannou K., Bauswein A., Clark J. A., 2020, *Phys. Rev. Lett.*, **125**, 261101
- Hempel M., Schaffner-Bielich J., 2010, *Nucl. Phys. A*, **837**, 210
- Hotokezaka K., Kyutoku K., Okawa H., Shibata M., Kiuchi K., 2011, *Phys. Rev. D*, **83**, 124008
- Hotokezaka K., Kiuchi K., Kyutoku K., Muranushi T., Sekiguchi Y.-i., Shibata M., Taniguchi K., 2013, *Phys. Rev. D*, **88**, 044026
- Iosif P., Stergioulas N., 2021, *MNRAS*, **503**, 850
- Kaplan J. D., Ott C. D., O'Connor E. P., Kiuchi K., Roberts L., Duez M., 2014, *ApJ*, **790**, 19
- Kastaun W., Galeazzi F., 2015, *Phys. Rev. D*, **91**, 064027
- Kastaun W., Ohme F., 2021, *Phys. Rev. D*, **104**, 023001
- Kastaun W., Ciolfi R., Giacomazzo B., 2016, *Phys. Rev. D*, **94**, 044060
- Kastaun W., Ciolfi R., Endrizzi A., Giacomazzo B., 2017, *Phys. Rev. D*, **96**, 043019
- Kiuchi K., Kyutoku K., Sekiguchi Y., Shibata M., 2018, *Phys. Rev. D*, **97**, 124039
- Koliogiannis P. S., Moustakidis C. C., 2021, *ApJ*, **912**, 69
- Komatsu H., Eriguchi Y., Hachisu I., 1989, *MNRAS*, **237**, 355

Table 7. Physical quantities for equilibrium remnant models constructed with the MPA1 EOS and different choices of rotation law parameters. The different quantities are defined as in Table 5.

r_p/r_e	$\epsilon_c (\times 10^{15})$	$\epsilon_{\max} (\times 10^{15})$	M	M_0	J	$T/ W $	Ω_c	Ω_{\max}	Ω_e	Ω_K	R_e	r_e	GRV3
$\{\lambda_1, \lambda_2\}$	$[\text{g cm}^{-3}]$	$[\text{g cm}^{-3}]$	$[M_\odot]$	$[M_\odot]$	$[\frac{GM_\odot^2}{c^3}]$		$[\text{rad/ms}]$	$[\text{rad/ms}]$	$[\text{rad/ms}]$	$[\text{rad/ms}]$	$[\text{km}]$	$[\text{km}]$	$(\times 10^{-5})$
{2.0, 0.5}													
0.3065	0.4260	0.5761	2.2	2.4131	4.4180	0.2205	8.4137	16.8274	4.2068	7.9797	17.1615	13.3944	14.4367
0.2985	0.4285	0.5925	2.3	2.5346	4.7867	0.2222	8.6843	17.3686	4.3421	8.1391	17.1622	13.2038	13.8202
0.2934	0.4350	0.6110	2.4	2.6578	5.1565	0.2232	8.9821	17.9643	4.4911	8.3202	17.1186	12.9678	13.4671
0.2911	0.4465	0.6324	2.5	2.7835	5.5263	0.2236	9.3157	18.6314	4.6578	8.5283	17.0270	12.6816	13.8714
0.2915	0.4641	0.6573	2.6	2.9123	5.8965	0.2234	9.6920	19.3842	4.8460	8.7668	16.8878	12.3448	9.5482
0.2936	0.4861	0.6855	2.7	3.0430	6.2685	0.2230	10.1113	20.2226	5.0556	9.0301	16.7122	11.9693	8.2679
0.2975	0.5140	0.7187	2.8	3.1769	6.6425	0.2221	10.5906	21.1815	5.2953	9.3294	16.4912	11.5439	7.1198
0.3042	0.5510	0.7608	2.9	3.3153	7.0144	0.2207	11.1621	22.3244	5.5811	9.6864	16.2037	11.0456	8.3531
0.3121	0.5970	0.8154	3.0	3.4568	7.3878	0.2190	11.8549	23.7102	5.9274	10.1095	15.8508	10.4744	8.6592
0.3224	0.6610	0.8970	3.1	3.6037	7.7617	0.2169	12.7936	25.5878	6.3968	10.6687	15.3706	9.7608	7.3993
0.3367	0.7900	1.0824	3.2	3.7578	8.1352	0.2144	14.6102	29.2249	7.3051	11.6946	14.4834	8.5922	8.1130
{1.5, 0.5}													
0.3866	0.5380	0.5819	2.2	2.4205	4.4179	0.2178	8.9666	13.4499	4.4833	8.0489	17.0026	13.2377	15.8326
0.3816	0.5485	0.5991	2.3	2.5424	4.7867	0.2196	9.2482	13.8723	4.6241	8.2177	16.9911	13.0347	12.0241
0.3788	0.5625	0.6187	2.4	2.6666	5.1565	0.2207	9.5562	14.3342	4.7781	8.4102	16.9350	12.7851	12.1648
0.3784	0.5805	0.6414	2.5	2.7934	5.5264	0.2210	9.8964	14.8445	4.9482	8.6295	16.8339	12.4881	12.2902
0.3795	0.6020	0.6671	2.6	2.9221	5.8966	0.2208	10.2697	15.4046	5.1349	8.8718	16.6965	12.1527	10.9684
0.3824	0.6280	0.6969	2.7	3.0541	6.2685	0.2200	10.6889	16.0334	5.3445	9.1453	16.5173	11.7716	8.2365
0.3866	0.6590	0.7321	2.8	3.1888	6.6425	0.2189	11.1632	16.7448	5.5816	9.4523	16.2976	11.3458	7.3561
0.3927	0.6980	0.7763	2.9	3.3274	7.0144	0.2173	11.7225	17.5838	5.8613	9.8135	16.0180	10.8541	7.8691
0.4004	0.7485	0.8350	3.0	3.4700	7.3878	0.2153	12.4110	18.6165	6.2055	10.2491	15.6659	10.2810	9.1894
0.4099	0.8240	0.9246	3.1	3.6177	7.7617	0.2129	13.3604	20.0406	6.6802	10.8311	15.1810	9.5587	7.8279
0.4228	1.0200	1.1673	3.2	3.7707	8.1352	0.2105	15.5006	23.2512	7.7503	12.0506	14.1554	8.2317	9.7803
{1.6, 1.0}													
0.4842	0.7127	0.7127	2.2	2.4349	4.4180	0.2026	5.5146	8.8233	5.5146	7.1943	18.1611	14.4404	14.5244
0.4872	0.7343	0.7343	2.3	2.5591	4.7867	0.2041	5.6713	9.0741	5.6713	7.4547	17.9811	14.0644	13.5309
0.4917	0.7588	0.7588	2.4	2.6855	5.1565	0.2048	5.8389	9.3422	5.8389	7.7359	17.7683	13.6528	12.4246
0.4974	0.7872	0.7872	2.5	2.8143	5.5264	0.2047	6.0192	9.6308	6.0192	8.0385	17.5258	13.2088	11.9574
0.5045	0.8206	0.8206	2.6	2.9460	5.8966	0.2040	6.2158	9.9452	6.2158	8.3660	17.2534	12.7314	11.2757
0.5125	0.8604	0.8604	2.7	3.0807	6.2686	0.2028	6.4319	10.2911	6.4319	8.7184	16.9557	12.2248	11.8631
0.5215	0.9088	0.9088	2.8	3.2183	6.6425	0.2012	6.6744	10.6790	6.6744	9.1027	16.6285	11.6841	11.0840
0.5322	0.9712	0.9712	2.9	3.3599	7.0144	0.1991	6.9594	11.1351	6.9594	9.5434	16.2476	11.0829	12.1694
0.5443	1.0582	1.0582	3.0	3.5061	7.3878	0.1967	7.3166	11.7066	7.3166	10.0705	15.7915	10.3956	13.0393

Landry P., Essick R., Chatziioannou K., 2020, *Phys. Rev. D*, **101**, 123007
Lucca M., Sagunski L., Guercilena F., Fromm C. M., 2021, *J. High Energy Astrophys.*, **29**, 19
Martynov D., et al., 2019, *Phys. Rev. D*, **99**, 102004
Miller M. C., et al., 2021, *ApJL*, **918**, L28
Möller P., Nix J., Kratz K.-L., 1997, *At. Data Nucl. Data Tables*, **66**, 131
Montaña G., Tolós L., Hanauske M., Rezzolla L., 2019, *Phys. Rev. D*, **99**, 103009
Most E. R., Weih L. R., Rezzolla L., Schaffner-Bielich J., 2018, *Phys. Rev. Lett.*, **120**, 261103
Müther H., Prakash M., Ainsworth T., 1987, *Phys. Lett. B*, **199**, 469
Oliver M., Keitel D., Miller A. L., Estelles H., Sintes A. M., 2019, *MNRAS*, **485**, 843
Page M. A., et al., 2021, *Commun. Phys.*, **4**, 27
Pang P. T. H., Tews I., Coughlin M. W., Bulla M., Van Den Broeck C., Dietrich T., 2021, *ApJ*, **922**, 14
Paschalidis V., Stergioulas N., 2017, *Living Rev. Relativ.*, **20**, 7
Paschalidis V., East W. E., Pretorius F., Shapiro S. L., 2015, *Phys. Rev. D*, **92**, 121502
Passamonti A., Andersson N., 2020, *MNRAS*, **498**, 5904
Raaijmakers G., et al., 2021, *ApJL*, **918**, L29
Radice D., 2020, *Symmetry*, **12**, 1249
Radice D., Perego A., Bernuzzi S., Zhang B., 2018, *MNRAS*, **481**, 3670
Radice D., Bernuzzi S., Perego A., 2020, *Annu. Rev. Nucl. Part. Sci.*, **70**, 95
Raithel C. A., Paschalidis V., Özel F., 2021, *Phys. Rev. D*, **104**, 063016

Riley T. E., et al., 2021, *ApJL*, **918**, L27
Rosati P., et al., 2021, *Exp. Astron.*,
Ruiz M., Shapiro S. L., Tsokaros A., 2021, *Front. Astron. Space Sci.*, **8**, 39
Sarin N., Lasky P. D., 2021, *Gen. Relativ. Gravit.*, **53**, 59
Sekiguchi Y., Kiuchi K., Kyutoku K., Shibata M., 2011, *Phys. Rev. Lett.*, **107**, 051102
Shibata M., Hotokezaka K., 2019, *Annu. Rev. Nucl. Part. Sci.*, **69**, 41
Steiner A. W., Hempel M., Fischer T., 2013, *ApJ*, **774**, 17
Stergioulas N., Friedman J. L., 1995, *ApJ*, **444**, 306
Stergioulas N., Apostolatos T. A., Font J. A., 2004, *MNRAS*, **352**, 1089
Stergioulas N., Bauswein A., Zagkouris K., Janka H.-T., 2011, *MNRAS*, **418**, 427
Studzinska A. M., Kucaba M., Gondek-Rosińska D., Villain L., Ansorg M., 2016, *MNRAS*, **463**, 2667
Szkudlarek M., Gondek-Rosińska D., Villain L., Ansorg M., 2019, *ApJ*, **879**, 44
Torres-Rivas A., Chatziioannou K., Bauswein A., Clark J. A., 2019, *Phys. Rev. D*, **99**, 044014
Tsang K. W., Dietrich T., Van Den Broeck C., 2019, *Phys. Rev. D*, **100**, 044047
Tsokaros A., Ruiz M., Shapiro S. L., 2020, *Phys. Rev. D*, **101**, 064069
Typel S., Röpke G., Klähn T., Blaschke D., Wolter H. H., 2010, *Phys. Rev. C*, **81**, 015803
Uryū K., Tsokaros A., Baiotti L., Galeazzi F., Taniguchi K., Yoshida S., 2017, *Phys. Rev. D*, **96**, 103011
Uryū K., Tsokaros A., Galeazzi F., Hotta H., Sugimura M., Taniguchi K.,

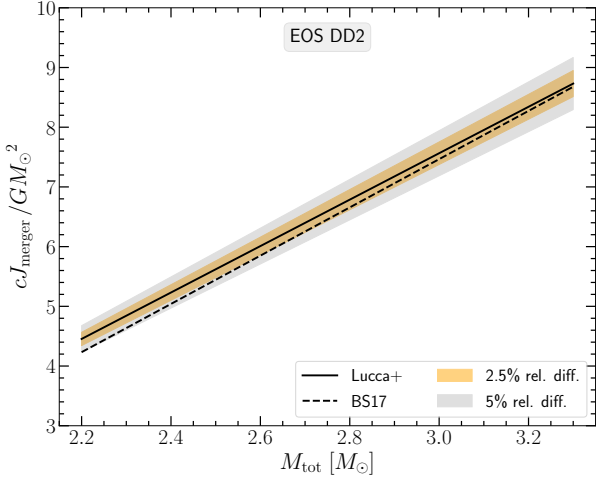


Figure A1. Comparison of empirical relations for the angular momentum at the time of merger, J_{merger} , vs. the total binary mass, M_{tot} , for the DD2 EOS. The solid line represents the empirical relation from [Lucca et al. \(2021\)](#) cast into the form used in [Bauswein & Stergioulas](#), i.e. equation (A1), while the dashed line represents the empirical relation from [Bauswein & Stergioulas \(2017\)](#), i.e. equation (7). The orange and grey filled areas denote the relative difference bands at the 2.5% and 5% level respectively.

Yoshida S., 2016, *Phys. Rev. D*, 93, 044056

Virtanen P., et al., 2020, *Nat. Methods*, 17, 261

Watts A. L., Andersson N., Jones D. L., 2005, *ApJ*, 618, L37

Weih L. R., Most E. R., Rezzolla L., 2018, *MNRAS*, 473, L126

Wiringa R. B., Fiks V., Fabrocini A., 1988, *Phys. Rev. C*, 38, 1010

Xie X., Hawke I., Passamonti A., Andersson N., 2020, *Phys. Rev. D*, 102, 044040

Yang H., Paschalidis V., Yagi K., Lehner L., Pretorius F., Yunes N., 2018, *Phys. Rev. D*, 97, 024049

Zhou E., Tsokaras A., Uryū K., Xu R., Shibata M., 2019, *Phys. Rev. D*, 100, 043015

APPENDIX A: COMPARISON OF ANGULAR MOMENTUM EMPIRICAL RELATIONS

In this appendix, we present a more detailed comparison for the empirical relations (7) and (8) discussed in Section 2.5, that were used to estimate the angular momentum at the time of merger.

As a first step, the [Lucca et al.](#) relation (8) is cast into the form used in [Bauswein & Stergioulas](#), i.e. it is expressed as a function of the total binary mass M_{tot} (for equal mass binaries, $M_{\text{NS}} = M_{\text{tot}}/2$)

$$\frac{cJ_{\text{merger}}}{GM_{\odot}^2} = \frac{a_1}{2} \left(\frac{R_{\text{NS}}}{GM_{\odot}} \right) \frac{M_{\text{tot}}}{M_{\odot}} + a_2 \left(\frac{R_{\text{NS}}}{c^2} \right)^2. \quad (\text{A1})$$

In Figure A1 the two angular momentum empirical relations (7) and (A1) are shown for the DD2 EOS. An M_{tot} ranging from $2.2M_{\odot}$ to $3.3M_{\odot}$ is assumed. Note that the threshold mass for prompt collapse to a black hole for this particular EOS is $M_{\text{thres}} \approx 3.325M_{\odot}$ as reported from numerical simulations by [Bauswein et al. \(2020, Supplementary Material\)](#). In equation (A1) we have set $R_{\text{NS}} = 13.1$ km, which is a typical circumferential radius value for progenitor neutron stars constructed with the DD2 EOS (see Figure 1). The two curves show very good agreement, deviating for the most part at the 2.5% level and at the 5% level only for very low mass remnants.

To investigate further the two angular momentum empirical formulas, we consider six zero-temperature, tabulated EOS, namely APR,

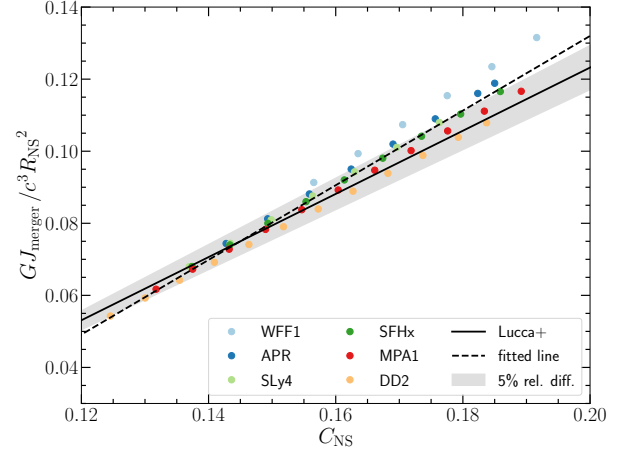


Figure A2. Angular momentum at the time of merger, J_{merger} , normalized by the TOV progenitor neutron star circumferential radius squared, R_{NS}^2 , vs. the corresponding compactness C_{NS} (equal mass binaries are assumed). The filled circles correspond to the data presented in Tables A1–A6, i.e. they represent J_{merger} predictions (normalized by R_{NS}^2) following the empirical formula in [Bauswein & Stergioulas \(2017\)](#) for remnants with different EOS and their correlation with the respective TOV progenitors' compactness C_{NS} . The dashed line is a linear fit to the filled circles data, i.e. equation (A2), the solid line represents the empirical formula of [Lucca et al. \(2021\)](#), i.e. equation (8), and the grey filled area the 5% relative difference band.

DD2 and MPA1 already mentioned in Section 2.4 with the addition of SFHx ([Steiner et al. 2013](#)), SLy4 ([Douchin & Haensel 2001](#)) and WFF1 EOS ([Wiringa et al. 1988](#)). For each EOS, we consider a remnant mass range starting from $2.2M_{\odot}$ and increasing with a step of $0.1M_{\odot}$ up to approximately the threshold mass value M_{thres} , as the latter is reported in [Bauswein et al. \(2020\)](#). Constructing the corresponding nonrotating progenitor models with $M_{\text{NS}} = M_{\text{tot}}/2$, we then use the empirical relations (7) and (8) to get predictions for the value of J_{merger} from each formula.

Tables A1, A2, A3, A4, A5 and A6 report the J_{merger} estimates from the [Bauswein & Stergioulas \(2017\)](#) and [Lucca et al. \(2021\)](#) expressions. For the EOS DD2, MPA1, SFHx and SLy4 excellent agreement is noticed, as the relative difference ranges from $\sim 0.5\%$ up to $\sim 5\%$. For the APR EOS, somewhat larger deviations ($> 6\%$) are noticed for remnants with masses over $2.6M_{\odot}$, with the [Bauswein & Stergioulas \(2017\)](#) approximate formula predicting larger angular momentum values. The picture is similar for the WFF1 EOS, with the deviations augmented to the 10% level.

In Figure A2, we compare the two empirical relations again, but this time focusing on the form of the [Lucca et al.](#) relation. Specifically, using the equilibrium progenitor models' calculated properties and assuming that the J_{merger} values follow equation (7), we investigate the correlation between $GJ_{\text{merger}}|_{\text{BS17}}/c^3 R_{\text{NS}}^2$ and C_{NS} . A linear fit of the same form as equation (8) is calculated

$$\frac{GJ_{\text{merger}}|_{\text{BS17}}}{c^3 R_{\text{NS}}^2} = b_1 C_{\text{NS}} + b_2, \quad (\text{A2})$$

with $b_1 = 1.0358 \pm 0.0265$ and $b_2 = -(7.517 \pm 0.429) \times 10^{-2}$ (1σ credible level). Note that (as expected) the errors in the coefficients of (8) are smaller, compared to our equilibrium model "hybrid" expression (A2). That said, both expressions are in very good agreement (at the 5% level) for the most part. Larger deviations are noticed between the two, only for the softer EOS, but these are gradually disfavored

Table A1. Angular momentum predictions from two different empirical relations, for the APR EOS. The total binary mass M_{tot} , the progenitor masses $M_{\text{NS}} = M_{\text{tot}}/2$, the equatorial circumferential radii R_{NS} and the values of compactness C_{NS} are shown. The J_{merger} columns correspond to angular momentum predictions from the empirical relations reported in [Bauswein & Stergioulas \(2017\)](#) (abbreviated as BS17) and [Lucca et al. \(2021\)](#) (abbreviated as Lucca+). The last column reports the absolute values of the relative difference between the J_{merger} predictions. Note that M_{tot} is terminated approximately at the M_{thres} value, as the latter is reported in [Bauswein et al. \(2020\)](#).

M_{tot} [M_{\odot}]	M_{NS} [M_{\odot}]	R_{NS} [km]	C_{NS}	$\frac{cJ_{\text{merger}}}{GM_{\odot}^2}$ [BS17]	$\frac{cJ_{\text{merger}}}{GM_{\odot}^2}$ [Lucca+]	rel. diff. [%]
2.20	1.10	11.3774	0.143	4.4165	4.3365	1.85
2.30	1.15	11.3735	0.149	4.8203	4.6733	3.14
2.40	1.20	11.3689	0.156	5.2248	5.0105	4.28
2.50	1.25	11.3634	0.162	5.6290	5.3469	5.28
2.60	1.30	11.3567	0.169	6.0324	5.6821	6.17
2.70	1.35	11.3482	0.176	6.4372	6.0175	6.97
2.80	1.40	11.3379	0.182	6.8417	6.3517	7.71
2.84	1.42	11.3331	0.185	7.0021	6.4838	7.99

Table A2. Same as Table A1 for the DD2 EOS.

M_{tot} [M_{\odot}]	M_{NS} [M_{\odot}]	R_{NS} [km]	C_{NS}	$\frac{cJ_{\text{merger}}}{GM_{\odot}^2}$ [BS17]	$\frac{cJ_{\text{merger}}}{GM_{\odot}^2}$ [Lucca+]	rel. diff. [%]
2.20	1.10	13.0385	0.125	4.2314	4.4513	4.94
2.30	1.15	13.0594	0.130	4.6361	4.8401	4.21
2.40	1.20	13.0795	0.135	5.0379	5.2273	3.62
2.50	1.25	13.0985	0.141	5.4448	5.6203	3.12
2.60	1.30	13.1161	0.146	5.8481	6.0109	2.71
2.70	1.35	13.1320	0.152	6.2519	6.4027	2.36
2.80	1.40	13.1460	0.157	6.6561	6.7954	2.05
2.90	1.45	13.1578	0.163	7.0607	7.1888	1.78
3.00	1.50	13.1672	0.168	7.4648	7.5818	1.54
3.10	1.55	13.1743	0.174	7.8683	7.9740	1.33
3.20	1.60	13.1784	0.179	8.2734	8.3673	1.12
3.28	1.64	13.1795	0.184	8.5960	8.6800	0.97

by the tightening astrophysical and nuclear constraints on the EOS of high density matter (see discussion in Section 2.4).

Overall, the agreement between the empirical formulas from [Bauswein & Stergioulas \(2017\)](#) and [Lucca et al. \(2021\)](#) at a level of a few per cent is notable, given that (i) they are independent analyses of different numerical simulations datasets and (ii) the formula appearing in [Bauswein & Stergioulas](#) was a benchmark for the DD2 EOS with an added approximate treatment to describe other EOS. In fact, since one cannot be certain that the specifics of the angular momentum extraction were performed in an identical way between the two works, the actual agreement could prove to be even better. In any case, an accuracy of a few per cent is adequate to get useful insights into merger remnants properties with equilibrium models.

This paper has been typeset from a $\text{\TeX}/\text{\LaTeX}$ file prepared by the author.

Table A3. Same as Table A1 for the MPA1 EOS.

M_{tot} [M_{\odot}]	M_{NS} [M_{\odot}]	R_{NS} [km]	C_{NS}	$\frac{cJ_{\text{merger}}}{GM_{\odot}^2}$ [BS17]	$\frac{cJ_{\text{merger}}}{GM_{\odot}^2}$ [Lucca+]	rel. diff. [%]
2.2	1.10	12.3276	0.132	4.3011	4.4180	2.65
2.3	1.15	12.3498	0.137	4.7060	4.7867	1.68
2.4	1.20	12.3711	0.143	5.1109	5.1565	0.88
2.5	1.25	12.3913	0.149	5.5146	5.5264	0.21
2.6	1.30	12.4102	0.155	5.9177	5.8966	0.36
2.7	1.35	12.4277	0.160	6.3217	6.2685	0.85
2.8	1.40	12.4437	0.166	6.7273	6.6425	1.28
2.9	1.45	12.4579	0.172	7.1300	7.0144	1.65
3.0	1.50	12.4702	0.178	7.5342	7.3878	1.98
3.1	1.55	12.4805	0.183	7.9387	7.7616	2.28
3.2	1.60	12.4885	0.189	8.3431	8.1352	2.56

Table A4. Same as Table A1 for the SFHx EOS.

M_{tot} [M_{\odot}]	M_{NS} [M_{\odot}]	R_{NS} [km]	C_{NS}	$\frac{cJ_{\text{merger}}}{GM_{\odot}^2}$ [BS17]	$\frac{cJ_{\text{merger}}}{GM_{\odot}^2}$ [Lucca+]	rel. diff. [%]
2.2	1.10	11.8206	0.137	4.3573	4.3801	0.52
2.3	1.15	11.8451	0.143	4.7619	4.7342	0.58
2.4	1.20	11.8649	0.149	5.1649	5.0877	1.52
2.5	1.25	11.8832	0.155	5.5700	5.4439	2.32
2.6	1.30	11.8965	0.161	5.9736	5.7989	3.01
2.7	1.35	11.9073	0.167	6.3775	6.1543	3.63
2.8	1.40	11.9140	0.173	6.7813	6.5092	4.18
2.9	1.45	11.9174	0.180	7.1856	6.8640	4.69
3.0	1.50	11.9151	0.186	7.5901	7.2173	5.17

Table A5. Same as Table A1 for the SLy4 EOS.

M_{tot} [M_{\odot}]	M_{NS} [M_{\odot}]	R_{NS} [km]	C_{NS}	$\frac{cJ_{\text{merger}}}{GM_{\odot}^2}$ [BS17]	$\frac{cJ_{\text{merger}}}{GM_{\odot}^2}$ [Lucca+]	rel. diff. [%]
2.2	1.10	11.8588	0.137	4.3833	4.3831	0.01
2.3	1.15	11.8421	0.143	4.7886	4.7341	1.15
2.4	1.20	11.8238	0.150	5.1916	5.0820	2.16
2.5	1.25	11.8033	0.156	5.5957	5.4292	3.07
2.6	1.30	11.7800	0.163	6.0007	5.7756	3.90
2.7	1.35	11.7537	0.170	6.4039	6.1181	4.67
2.8	1.40	11.7239	0.176	6.8078	6.4588	5.40

Table A6. Same as Table A1 for the WFF1 EOS.

M_{tot} [M_{\odot}]	M_{NS} [M_{\odot}]	R_{NS} [km]	C_{NS}	$\frac{cJ_{\text{merger}}}{GM_{\odot}^2}$ [BS17]	$\frac{cJ_{\text{merger}}}{GM_{\odot}^2}$ [Lucca+]	rel. diff. [%]
2.2	1.10	10.3754	0.157	4.5093	4.2029	7.29
2.3	1.15	10.3840	0.164	4.9126	4.5119	8.88
2.4	1.20	10.3911	0.171	5.3178	4.8225	10.27
2.5	1.25	10.3970	0.178	5.7222	5.1326	11.49
2.6	1.30	10.4010	0.185	6.1260	5.4420	12.57
2.7	1.35	10.4034	0.192	6.5297	5.7512	13.54